THZ SPECTROSCOPY OF CRYSTALS:

ULTRAFAST DYNAMICS,

NON-RECIPROCITY & SYMMETRY

BREAKING

AN ABSTRACT

SUBMITTED ON THE TWENTY-EIGHTH DAY OF APRIL, 2022

TO THE DEPARTMENT OF PHYSICS AND ENGINEERING PHYSICS

IN PARTIAL FULFILLMENT OF THE REQUIREMENTS OF THE SCHOOL OF

SCIENCE AND ENGINEERING OF TULANE UNIVERSITY FOR THE DEGREE OF
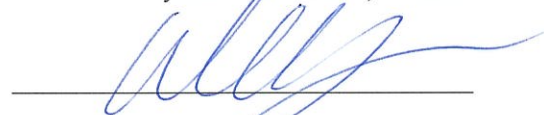
DOCTOR OF PHILOSOPHY

BY

_____

XIAOJIANG LI

APPROVED BY:

_____

DIYAR TALBAYEV, PH.D.

_____

JIANWEI SUN, PH.D.

_____

WEI JIANG, PH.D.

Abstract

Terahertz radiation band is crowded with spectral features of many fundamental physical processes, such as molecular rotations, lattice vibrations, intraband transitions, superconducting gaps, etc. This property makes THz spectroscopy a powerful tool for the investigation of novel properties in new materials. In this thesis, I will start from the introduction of basic knowledge of mathematics and physics related to spectroscopy, including group and representation theories, the character tables, classification of crystal lattices, 32 point groups, non-linear optics, infrared and Raman mode, optical activity, symmetry breaking, SOS, magnetic materials and various magnetic interactions. Then I will introduce different THz spectroscopy that are commonly used in our lab, focusing on different THz generation and detection methods, followed by the data analysis processes for the extraction of various optical parameters of crystals. At last, I will discuss the three different kinds of materials that I studied during my Ph.D career: quantum paraelectric perovskite crystal $KTaO_3$, chiral stuffed tridymite crystal $BaCoSiO_4$ and ferrimagnetic spinel crystal $FeMnO_4$. In the three materials, I will discuss THz field-induced SHG, THz Kerr effect, optical non-reciprocity, symmetry operational similarity, optical activity and field induced birefringence respectively. . . .

THZ SPECTROSCOPY OF CRYSTALS:

ULTRAFAST DYNAMICS,

NON-RECIPROCITY & SYMMETRY

BREAKING

A DISSERTATION

SUBMITTED ON THE TWENTY-EIGHTH DAY OF APRIL, 2022

TO THE DEPARTMENT OF PHYSICS AND ENGINEERING PHYSICS

IN PARTIAL FULFILLMENT OF THE REQUIREMENTS OF THE SCHOOL OF

SCIENCE AND ENGINEERING OF TULANE UNIVERSITY FOR THE DEGREE OF

DOCTOR OF PHILOSOPHY

BY

_____

XIAOJIANG LI

APPROVED BY:

_____

DIYAR TALBAYEV, PH.D.

_____

JIANWEI SUN, PH.D.

_____

WEI JIANG, PH.D.

Acknowledgements

Contents

Contents

Contents

List of Figures

List of Tables

Chapter 1

Group, representation and character table

Symmetry operations of crystals, elementary particles, fields all possess the properties of mathematical group. Here as a review, I summarized the basic concepts of group theory related to spectroscopy based on the reference [1, 2].

1.1 Group

Let G be a set together with a binary operation (usually called multiplication) that assigns to each ordered pair (a, b) of elements of G an element in G denoted by ab. We say G is a group under this operation if the following three properties are satisfied.

1. Associativity. The operation is associative; that is, $(ab)c = a(bc)$ for all a, b, c in G.

2. Identity. There is an element e(called the identity) in G such that $ae = ea = a$ for all a in G.

3. Inverses. For each element a in G, there is an element b in G (called an inverse of a) such that $ab = ba = e$[3].

Here the element a, b, c in group G represent symmetry operations in crystals in this article.

A subgroup is just a group within a group. The order of any subgroup must be an integral divisor of the order of the main group.

A similarity transformations is defined by the consecutive application of three operations a, b, c, where a, b, c are any operations:

$$b^{-1}ab = c \qquad (1.1)$$

Here a and c related by a similarity transformation are said to be conjugate.

A class is a complete set in a group which all the operators in the set are conjugate to one another. The identity operator E is always in a class by itself, so are the same with inversion operation$\bar{1}$ and horizontal mirror plane σ_h. The order of a class must be an integral divisor of the order of the group, but not all integral divisor must exist as a class.

1.2 Irreducible representations

Symmetry operations can be represented by infinite number of multiple dimensional square matrices. By using similarity transformations, one can reduce matrices into block diagonal matrices, and each block of the bigger matrix follows the same multiplication table of the bigger one, and thus can work as a new representation of the same symmetry operation.

When a bigger matrix can not be further reduced by similarity transformations, each block of the bigger matrix are called irreducible representations, Γ_i. Although the number of reducible representations is infinite, the number of irreducible representations of most point groups are finite and small, it equals to the number of classes in the group. Suppose a group of order g has precisely k non-equivalent irreducible representations,$\Gamma_i^{(1)}, \Gamma_i^{(2)}, \ldots, \Gamma_i^{(k)}$, then the dimensions $d_1, d_2, \ldots, d_k$ of these irreducible representations satisfy:

$$d_1^2 + d_2^2 + \cdots + d_k^2 = g \qquad (1.2)$$

It is found that for any point group there is only one set of k integers that satisfy equation 1.2, thus the numbers and the dimensions of irreducible representations for every group can be uniquely determined.

TABLE 1.1: Complete C_{4v} character table[4]

C_{4v}	E	$2C_4$ (z)	C_2	$2\sigma_v$	$2\sigma_d$	linear functions, rotations	quadratic functions	cubic functions
A_1	+1	+1	+1	+1	+1	z	x^2+y^2, z^2	$z^3, z(x^2+y^2)$
A_2	+1	+1	+1	-1	-1	R_z	-	-
B_1	+1	-1	+1	+1	-1	-	x^2-y^2	$z(x^2-y^2)$
B_2	+1	-1	+1	-1	+1	-	xy	xyz
E	+2	0	-2	0	0	$(x, y) (R_x, R_y)$	(xz, yz)	$(xz^2, yz^2) (xy^2, x^2y) (x^3, y^3)$

1.3 Character table

The trace of a matrix is also called character. The characters of any operations in the same class are the same, and they are independent of the choice of coordinates.

A character table lists all the possible operations of a symmetry group as shown in the C_{4v} character table 1.1 for example. The most left column of the table are the Mulliken symbles of the irreducible representations. Conventionally for the finite group, *A* and *B* denote one-dimensional representations, *E* denotes two-dimensional and *T* denotes three-dimensional. The character of the identity operation *E* is always the dimension of the irreducible representation. The difference between *A* and *B* is that the character of the principle rotation C_n is always $+1$ for *A* and -1 for *B*. The subscripts *g* and *u* represent symmetric and antisymmetric representations with respect to inversion operation. While the superscripts ′ and ″ denote symmetric and antisymmetric representations with respect to σ_h. The three columns on the right hand side of the table represent the basic function, which will be heavily used in the selection rules later on.

The decomposition of any reducible representation is unique, knowing the reducible representation of a group, one can easily figure out the compositing irreducible representations by inspection or the decomposition equation below:

$$a_i = (1/h) \sum_R (\chi^R \cdot \chi_i^R \cdot C^R) \tag{1.3}$$

Where a_i is the number of the irreducible representation Γ_i in the reducible representation Γ_{red}, *h* is the order of the point group, *R* is an operation of the group,

χ^R is the character of the operation R in the reducible representation Γ_{red}, χ_i^R is the character of the operation R in the irreducible representation Γ_i, C^R is the number of members in the class to which R belongs.

So far, we only discussed the representations of symmetry operations in crystals, but in spectroscopy, what we are actually measuring are the resonances of the normal modes of vibration with the optical probe, the following statement establishes the connections in between: each normal mode of vibration will form a basis for a irreducible representation of the point group of lattice.

The procedure to find the irreducible representations of normal mode of molecule vibration is summarized below:

1.Assign x,y,z coordinates to each atom.

2.Determine how each axis transforms for every class of symmetry operation in the group.

If an atom moves, the character for all of its axes is 0.

If an atom is stationary and the axis direction is unchanged, its character is 1.

If an atom is stationary and the axis direction is reversed, its character is -1

3.Sum the characters in each class to determine the reducible representation Γ_{red}.

4.Reduce Γ_{red} to its irreducible components using the character table and equation 1.3.

5.Use the character table to subtract the translations and rotations, leaving the representations corresponding to the vibrations.

1.4   Transition integral in spectroscopy

The exact wave function solutions of the molecular vibrational wave equations under harmonic approximation can be write as the products of Hermite polynomials and the corresponding energy levels are:

$$E_{k,n_k} = \hbar\omega_k(n_k + \frac{1}{2}) \tag{1.4}$$

Where ω_k is identical to the classical frequency of the kth normal mode. $n_k = 0, 1, 2, \ldots$ is the vibrational quantum number of kth mode. It should be noted that the vibrational modes are bosons, excitation of particular mode only increases the number of phonons with the same frequency but changes the parity of the corresponding wave function.

In absorption spectroscopy, the interaction of EM wave $\boldsymbol{E} = \boldsymbol{E_0}cos(\omega t)$ with the electric dipole moment of the materials introduces the time dependent perturbation to the system after $t = 0$:

$$H' = \mathbf{p} \cdot \mathbf{E} \tag{1.5}$$

The Hamiltonian of the whole system can be written as:

$$H = H^0 + H' \tag{1.6}$$

Where H^0 is the Hamiltonian of the system at $t = 0$. From the time-dependent perturbation theory one knows that the solutions of the Schrödinger's equation can be written as a series of non-perturbed time-independent wave functions:

$$\Psi(t) = \sum c_n(t)\psi_n e^{-iE_n t/\hbar} \tag{1.7}$$

After a few steps of derivations, the transition rate of the system from state n to m can be written as:

$$\Gamma = c_m^*(t)c_m(t) = \frac{E_0^2}{4\hbar^2}[< m|p_x|n >^2 + < m|p_y|n >^2 + < m|p_z|n >^2] \tag{1.8}$$

Where the part within the square bracket in equation 1.8 is called *transition moment integral*, denoted by M_{nm}^2. Because the dipole moment is independent of the translational integral, and the rotational integral is constant, one only needs to consider the vibrational part in the transition moment integral. Considering

the harmonic approximation of the integral, one can readily derive the vibrational selection rules: $\Delta n_k = \pm 1$, but more general selection rules can be found by symmetry analysis of the transition moment integral.

1.5 Selection rules

Transitions observed in IR spectrum are infrared active, a vibrational transition is infrared active if the dipole moment $\hat{p}$ changes during this process. Transitions observed in the Raman spectrum are Raman active, a vibrational transition is Raman active if the polarizability $\hat{\alpha}$ changes during this process. The transition probability is determined by the transition integral from equation 1.8. Let's take x component as an example, write the transition integral in a more general way:

$$M^2_{nm} = | < m|\hat{Q}|n > |^2 \tag{1.9}$$

Where $\hat{Q}$ can be the dipole moment or polarizability. The transition integral can only have nonzero value if the direct product of the irreducible representation of each component of the integrand contains the totally symmetric irreducible representation of the point group, therefore, by studying the symmetries of the initial, final states and the $\hat{Q}$ operator, one can predict if the transition is allowed or forbidden.

The irreducible representations for $\hat{Q}$ can be readily read from the character table. The irreducible representations of dipole moment correspond to the rows with x, y, z components in the linear function column in table 1.1, while the irreducible representations of polarizability correspond to the rows with x^2, y^2, z^2, xy, xz, yz components in the quadratic functions column.

Thus far, one has acquired all the ingredients needed to understand the transitions in the IR and Raman spectroscopy. Lastly, an useful fact for central symmetric materials: $\hat{p}$ will always have u symmetry, while $\hat{\alpha}$ will always have g symmetry, therefore the IR active modes and Raman active modes are mutual exclusive in materials with inversion center.

Chapter 2

Crystallography

A Bravais lattice is an infinite array of discret points with an arrangement and orientation that appears *exactly* the same, from whichever of the points the array is viewed[5].

Any symmetry operations in Bravais lattice can be decomposed into translation T_R and a rigid operation leaving at least one lattice point fixed which forms a point group. Considering the point group of Bravais lattice, one gets 7 crystal systems and 32 crystallographic point groups including the symmetry of basis. Considering the full symmetry of the Bravais lattice, one gets 14 Bravais lattice and 230 space groups including the symmetry of basis (73 symmorphic space groups) plus screw axes and glide planes (157 nonsymmorphic space groups).

2.1 Crystal lattice

The seven crystal systems are classified with respect to the metrics and symmetries as shown in table 2.1. The trig- and hexagonal crystal systems are subsumed to the hexagonal crystal family because their unit cell shapes are identical. But the symmetry of the motif (basis) in trigonal system is only three-fold rather than six-fold in hexagonal system. Interestingly, the hexagonal crystal family can also be divided into hexagonal and rhombohedral lattice systems while the trigonal crystal system is not equivalent to the rhombohedral lattice system[6].

TABLE 2.1: Seven crystal systems[6]

Crystal system	Restrictions concerning the		Maximal symmetry
	Length of axes	Angles of the cell	
Triclinic	*None*[a]	*None*[a]	$\bar{1}$
Monoclinic	*None*[a]	$\alpha = \gamma = 90°$	$2/m$
Orthorhombic	*None*[a]	$\alpha = \beta = \gamma = 90°$	mmm
Tetragonal	$a = b$	$\alpha = \beta = \gamma = 90°$	$4/mmm$
Trigonal	$a = b$	$\alpha = \beta = 90°, \gamma = 120°$	$\bar{3}/m$
Hexagonal	$a = b$	$\alpha = \beta = 90°, \gamma = 120°$	$6/mmm$
Cubic	$a = b = c$	$\alpha = \beta = \gamma = 90°$	$m\bar{3}m$

[a]This means that the respective parameters can have any conceivable value

2.2 Nomenclature of 32 point groups

The Schoenflies and the international nomenclatorial systems are both in wide use. The designations of the 32 point groups of both are shown in table 2.2 and table 2.3.

The meaning of the Schoenflies notation:

C_n : Groups contain an n-fold rotation axis.

C_{nv} : Groups contain n-fold axis and as many mirror planes that contain the n-fold rotation axis as it requires.

C_{nh} : Groups contain n-fold axis and a single mirror plane perpendicular to the axis.

S_n : Groups contain only an n-fold rotation-reflection axis.
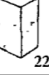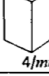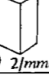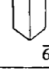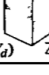
D_n : Groups contain an n-fold rotation axis and as many 2-fold axes perpendicular to the n-fold axis as it requires.

D_{nh} : Groups contain all the elements in D_n and a mirror plane perpendicular to the n-fold axis.

D_{nd} : Groups contain all the elements of D_n and mirror planes containing the n-fold axis, which bisect the angles between the 2-fold axes.

O_h : Full symmetry group of the cube including improper operations, which the horizontal reflection plane (h) admits.

TABLE 2.2: The noncubic crystallographic point groups[5]

O : Cubic group without improper operations.

T_d : Full symmetry group of the regular tetrahedron including all improper operations.

T : Tetrahedron group excluding improper operations.

T_h : Results when an inversion is added to T.

Any operation that takes a right-handed object into a left-handed one is called improper, that is operations containing an odd number of inversions or mirror reflections are improper.

The international notation consists of a maximum of four symbols for each space group. For example, the crystal structure of $KTaO_3$ is $Pm\bar{3}m$ No. 221,

TABLE 2.3: The cubic crystallographic point groups[5]
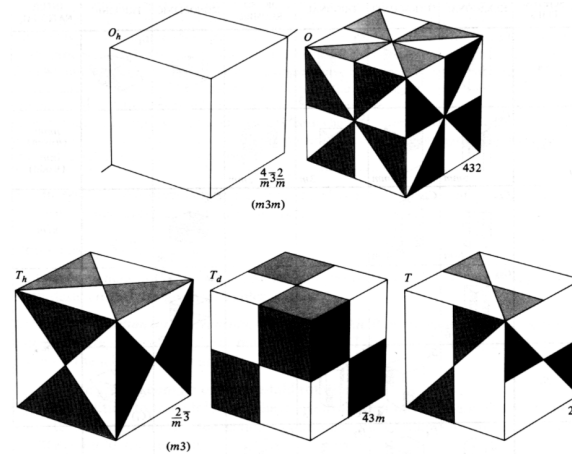
TABLE 2.4: Viewing directions for the seven crystal systems[6]

Crystal system	Viewing directions		
Triclinic	*none*		
Monoclinic	*b (c)*[a]	–	–
Orthorhombic	*a*	*b*	*c*
Tetragonal	*c*	*a*	[110]
Trigonal	*c*	*a*	–
Hexagonal	*c*	*a*	[210]
Cubic	*c*	[111]	[110]

[a]In the monoclinic crystal system, symmetry elements can only appear in one direction; by convention this should be the *b* direction; however, in some countries, especially in Eastern Europe, the *c* direction is used instead

which belongs to cubic structure O_h. The first letter indicates the centering of the Bravais type, here 'P' is for primitive which means 'not centered', while 'I' is for body-centered, 'C' for one-side face centered and 'F' for all-side face centered. The following three letters indicate symmetries along three viewing directions which are summarized in table 2.4 for seven crystal systems. The second letter 'm' indicates mirror reflection found in the viewing direction along c for cubic structure. The third letter '$\bar{3}$' indicates three-fold rotation plus inversion symmetry along [111] direction and the last 'm' indicates another mirror reflection perpendicular to [110] direction.

Another example for the international notation is the tetragonal structure $FeMn_2O_4$ with the space group $I4_1/amd$ No. 141 which we also studied in this thesis. The viewing direction for tetragonal structure is c, a, [110], table 2.4. In the structure

notation of this crystal, 'I' is for body-centered. '$4_1/a$' represents four-fold rotation axis plus 1/4 lattice constant translation along c-direction plus a-directional 1/2 lattice constant glide plane which perpendicular to c-direction. 'm' represents mirror plane perpendicular to a direction. 'd' represents diamond glide plane perpendicular to [110] direction.

Chapter 3

Classical models of optical medium

3.1 Permittivity and conductivity

We start from macroscopic Maxwell equations to study the light-matter interactions, since in most cases, the electromagnetic wave length is much longer the microscopic scales of the media, the microscopic field is averaged over distance. As a review, the Maxwell equations is listed in the following form:

$$
\begin{aligned}
(i) & \nabla \cdot \mathbf{D} = \rho_{ext} \\
(ii) & \nabla \cdot \mathbf{B} = 0 \\
(iii) & \nabla \times \mathbf{E} = -\frac{\partial \mathbf{B}}{\partial t} \\
(iv) & \nabla \times \mathbf{H} = \mathbf{J}_{ext} + \frac{\partial \mathbf{D}}{\partial t}
\end{aligned}
\tag{3.1}
$$

where $\mathbf{D} = \epsilon_0 \mathbf{E} + \mathbf{P} = \epsilon_0 \epsilon \mathbf{E}$ and $\mathbf{H} = \frac{1}{\mu_0} \mathbf{B} - \mathbf{M} = \mu_0 \mu \mathbf{H}$ are the constitutvie equations. Here in the Maxwell equations, we distinguish between external $(\rho_{ext}, \mathbf{J}_{ext})$ and internal $(\rho, \mathbf{J})$ charge and current densities in order to avoid the confusion of the application of boundary conditions. In non-magnetic materials, the relative permeability μ is assumed to be 1. By considering the non-locality in time and space, one can generalize the constitutive equations into[7]:

$$
\begin{aligned}
\mathbf{D}(\mathbf{r}, t) &= \epsilon_0 \int dt' \mathbf{dr}' \epsilon(\mathbf{r} - \mathbf{r}', t - t') \mathbf{E}(\mathbf{r}', t') \\
\mathbf{J}(\mathbf{r}, t) &= \int dt' \mathbf{dr}' \sigma(\mathbf{r} - \mathbf{r}', t - t') \mathbf{E}(\mathbf{r}', t')
\end{aligned}
\tag{3.2}
$$

By applying the convolution theorem on equation 3.2, one gets the frequency domain constitutive equations:

$$\mathbf{D}(\mathbf{K}, \omega) = \epsilon_0 \epsilon(\mathbf{K}, \omega) \mathbf{E}(\mathbf{K}, \omega)$$
$$\mathbf{J}(\mathbf{K}, \omega) = \sigma(\mathbf{K}, \omega) \mathbf{E}(\mathbf{K}, \omega) \tag{3.3}$$

Combine with the equation $\mathbf{J} = \frac{\partial \mathbf{P}}{\partial t}$, one gets the fundamental relation between permittivity and conductivity:

$$\epsilon(\mathbf{K}, \omega) = 1 + \frac{i\sigma(\mathbf{K}, \omega)}{\epsilon_0 \omega} \tag{3.4}$$

The complex permittivity of material can be figured out experimentally by determining the complex refractive index $\tilde{n}(\omega) = n(\omega) + i\kappa(\omega) = \sqrt{\epsilon}$, therefore, one can get the conductivity of the material from equation 3.4. κ is the extinction coefficient which describes the absorption of the electromagnetic wave propagating in the medium.

The attenuation of electromagnetic wave propagating in the medium is described by equation:

$$I(x) = I_0 e^{-\alpha x} \tag{3.5}$$

where *alpha* is the absorption coefficient related to the extinction coefficient κ.

$$\alpha(\omega) = \frac{2\kappa(\omega)\omega}{c} \tag{3.6}$$

3.2   Lorentz and Drude model

For the light-matter interactions, classical Lorentz model provide a good qualitative description for bound electrons. Considering the motion of harmonic oscillator, the energy of the system can be written as $U(x) = \frac{1}{2}\omega_0^2 x^2$, where ω_0 is the resonance frequency, the driving field is monochromatic wave $E(t) = E_0 e^{-i\omega t}$, then the motion of the electron can be expressed as:

$$\frac{d^2x}{dt^2} + \gamma\frac{dx}{dt} + \omega_0^2 x = \frac{q}{m}E(t) \tag{3.7}$$

Where γ is the damping constant. The solution of the equation of motion is:

$$x(t) = \frac{q}{m}\frac{E_0}{\omega_0^2 - \omega^2 - i\omega\gamma}e^{-i\omega t} \tag{3.8}$$

Therefore the relative permittivity can be expressed as:

$$\epsilon_r(\omega) = 1 + \chi_e(\omega) = 1 + \frac{Nq^2}{m\epsilon_0}\frac{1}{\omega_0^2 - \omega^2 - i\omega\gamma} \tag{3.9}$$

Where N is the density of electrons. By setting the resonance frequency $\omega_0 = 0$, one can get the solution for the free electrons which is Drude model:

$$\epsilon_r(\omega) = 1 + \chi_e(\omega) = 1 - \frac{Nq^2}{m\epsilon_0}\frac{1}{\omega^2 + i\omega\gamma} = 1 - \frac{\omega_0}{\omega^2 + i\omega\gamma} \tag{3.10}$$

Where $\omega_0 = \sqrt{\frac{Nq^2}{m\epsilon_0}}$ is the plasma frequency, usually metals become transparent above ω_0. A typical electron density $10^{16}cm^{-3}$ for semiconductors corresponding to $\omega_p \approx 6THz$[8].

Chapter 4

Nonlinear optics

Nonlinear optics is the study of the modifications of the optical properties of materials under the presence of high-power laser. By neglecting the vector nature of polarization **P** firstly, and assuming the medium responds instantaneously (lossless and dispersionless), we can expand the nonlinear response of materials as a series of external electric field **E** including the first linear term as following:

$$P(t) = P^{(1)}(t) + P^{(2)}(t) + P^{(3)}(t) + \cdots$$
$$= \epsilon_0(\chi^{(1)}E(t) + \chi^{(2)}E^2(t) + \chi^{(3)}E^3(t) + \cdots)$$

(4.1)

Where $\chi^{(2)}$ and $\chi^{(3)}$ are the second- and third-order nonlinear susceptibilities respectively.

By considering the vector nature of the polarization, we can see that $\chi^{(1)}$, $\chi^{(2)}$ and $\chi^{(3)}$ become second-,third- and forth-rank tensors. For example:

$$P_i^{(2)} = \epsilon_0 \sum_{j,k} \chi_{ijk}^{(2)} E_j E_k$$

(4.2)

$$P_i^{(3)} = \epsilon_0 \sum_{j,k,l} \chi_{ijkl}^{(2)} E_j E_k E_l$$

(4.3)

Where $\{i, j, k, l\} \in \{x, y, z\}$. Many of these terms in the nonlinear susceptibilities are the same or zero due to the symmetry of the crystals.

Second-order nonlinear effect is only allowed in noncentrosymmetric materials such as ZnTe, GaP and LiNbO$_3$. Optical rectification, Pockels effect and Second harmonic generation (SHG) are all very important second-order nonlinear effects.

Third-order nonlinear effect is particularly important in isotropic media, such as gases, liquids and glasses. Optical Kerr effect, Ramman scattering and frequency tripling are important third-order nonlinear effects.

4.1 Second-harmonic generation (SHG)
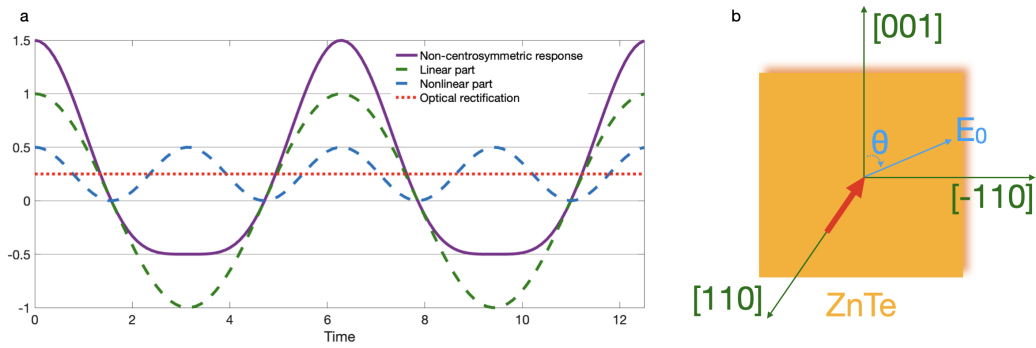
FIGURE 4.1: (a) Decomposition of second-order nonlinear effect. (b) Optical rectification of ZnTe crystal.

The sinusoidal electric field of the optical beam can be represented as:

$$E(t) = Ee^{-i\omega t} + E^* e^{i\omega t} \tag{4.4}$$

By plugging equation 4.4 into the second-order nonlinear term in equation 4.1, we get:

$$P^{(2)}(t) = 2\epsilon_0 \chi^{(2)} EE^* + \epsilon_0 \chi^{(2)} (E^2 e^{-i2\omega t} + E^{*2} e^{i2\omega t}) \tag{4.5}$$

The zero frequency term on the right-hand side is know as optical rectification by which a static electric field is created within the nonlinear crystal, see the red dotted line in figure 4.1(a). While the second term has a frequency 2ω is the second-harmonic generation, see the cyan dashed line in figure 4.1(b). SHG is broadly used in laser generation, microscopy and spectroscopy. For example, SHG in KDP is used to transfer 1064 nm infrared light generated from Nd:YAG laser to 532 nm green light in laser industry.

4.2 Optical rectification

By writing the second-order nonlinear susceptibility of the optical rectification term of equation 4.5 in tensor form we get:

$$P_i^{(2)}(0) = \sum_{j,k} \epsilon_0 \chi_{ijk}^{(2)}(0,\omega,-\omega) E_j(\omega) E_k^*(\omega) \tag{4.6}$$

Given the indices are permutable and considering the contracted matrix, equation 4.6 can be written as:

$$\begin{bmatrix} P_x \\ P_y \\ P_z \end{bmatrix} = 2\epsilon_0 \begin{bmatrix} d_{11} & d_{12} & d_{13} & d_{14} & d_{15} & d_{16} \\ d_{21} & d_{22} & d_{23} & d_{24} & d_{25} & d_{26} \\ d_{31} & d_{32} & d_{33} & d_{34} & d_{35} & d_{36} \end{bmatrix} \begin{bmatrix} E_x^2 \\ E_y^2 \\ E_y^2 \\ 2E_yE_z \\ 2E_zE_x \\ 2E_xE_y \end{bmatrix} \tag{4.7}$$

By plugging in the corresponding contracted matrix for certain material, one is alowed to calculate the response from optical rectification. For example in ZnTe, by aligning the polarization direction of the incident light along $[\bar{1}11]$ direction, which is the chemical bonds between the Zn and Te atoms, the generated THz light is maximized, figure 4.1(b).

4.3 Pockels effect

Induced optical anisotropy is quite ubiquitous in crystals, strain induced anisotropy is call photo-elastic effect, magnetic field induced circularly birefringence is the Faraday effect, and electric field induced birefringence such as Pockels effect and optical Kerr effect which are the main topics in the current and following section.

Pockels effect is a second-order nonlinear effect as shown in equation 4.8, while the optical Kerr effect is the third-order nonlinear effect as shown in equation 4.9. Pockels effect happens in anisotropic crystals, while optical Kerr effect is observed in isotropic crystals in which second-order nonlinear effect is symmetrically forbidden.

The response of the nonlinear materials for Pockels effect is described as:

$$P_i^{(2)}(\omega) = 2\sum_{j,k}\epsilon_0\chi_{ijk}^{(2)}(\omega,\omega,0)E_j(\omega)E_k(0) = \sum_j\epsilon_0\chi_{ij}^{(2)}(\omega)E_j(\omega) \tag{4.8}$$

where $\chi_{ij}^{(2)}(\omega) = 2\sum_k\chi_{ijk}^{(2)}(\omega,\omega,0)E_k(0)$ is the field induced susceptibility tensor, and $E_k(0)$ is the external *dc* electric field.

In the free-space electro-optic sampling method, one utilizes Pockels effect to detect the THz field-induced refractive index changes, by knowing the change of the refractive index in linear range, one can map out the waveform of the transmitted THz beam. For example, one of the most commonly used crystals is ZnTe and the corresponding matrix equation is:

$$
\begin{bmatrix} P_x \\ P_y \\ P_z \end{bmatrix} = 4\epsilon_0 d_{14}
\begin{bmatrix} 0 & 0 & 0 & 1 & 0 & 0 \\ 0 & 0 & 0 & 0 & 1 & 0 \\ 0 & 0 & 0 & 0 & 0 & 1 \end{bmatrix}
\begin{bmatrix} E_{O,x}E_{THz,x} \\ E_{O,y}E_{THz,y} \\ E_{O,z}E_{THz,z} \\ E_{O,y}E_{THz,z} + E_{O,z}E_{THz,y} \\ E_{O,z}E_{THz,x} + E_{O,x}E_{THz,z} \\ E_{O,x}E_{THz,y} + E_{O,y}E_{THz,x} \end{bmatrix}
$$

4.4 Optical Kerr effect

The response of nonlinear materials for optical Kerr effect is described as:

$$P_i^{(3)}(\omega) = 3\sum_{j,k,l}\epsilon_0\chi_{ijkl}^{(3)}(\omega,\omega,0,0)E_j(\omega)E_k(0)E_l(0) = \sum_j\epsilon_0\chi_{ij}^{(3)}(\omega)E_j(\omega) \tag{4.9}$$

where $\chi_{ij}^{(3)}(\omega) = 3\sum_{k,l}\chi_{ijkl}^{(3)}(\omega,\omega,0,0)E_k(0)E_k(0)$ is the field induced susceptibility tensor.

The electric permittivity of the nonlinear materials can be described by:

$$\epsilon_r^{nl} = 1 + \chi^{(1)} + \chi^{(3)} E^2 = \epsilon_r + \Delta\epsilon \tag{4.10}$$

where $\epsilon_r = 1 + \chi^{(1)}$ and $\Delta\epsilon = \chi^{(3)} E^2$. For non-absorbing medium, the refraction index is equal to the square root of the relative permittivity, thus we have:

$$n = (\epsilon_r + \Delta\epsilon)^{1/2} \approx \sqrt{\epsilon_r} + \frac{\Delta\epsilon}{2\sqrt{\epsilon_r}} = n_0 + \Delta n \tag{4.11}$$

where we assumed that $\Delta\epsilon << \epsilon_r$ and we split the refractive index into its linear part $n_0 = \sqrt{\epsilon_r}$ and nonlinear part Δn. By plugging in the relation $\Delta\epsilon = \chi^{(3)} E^2$ and considering THz beam as the pump beam, we get:

$$n(I^{THz}) = n_0 + \frac{\chi^{(3)}(\omega_{THz}, \omega_{THz}, \omega)}{2n_0}(E^{THz})^2 = n_0 + n_2 I^{THz} \tag{4.12}$$

From equation 4.12 we can see that the change of refractive index in the optical Kerr effect is proportional to the intensity of the incident THz light.

Chapter 5

Phonon and scattering

In contrast to the optical properties of bound electrons, which occur at visible and ultraviolet frequencies, the interactions of phonons in a crystal with light turn out to be in the infrared region. In this section, we will discuss the Infrared spectroscopy which is the direct interactions of phonon dipoles with EM wave, and the inelastic scattering including Raman scattering and Brilloin scattering. The Raman scattering arises from the change of refraction index by the optical phonons while the Brilloin scattering is by the acoustic phonons.

5.1 Infrared active phonon

The EM wave can only directly couple with ionic crystals or covalent crystals with polar bounds. None of the optical phonons of the purely covalent crystal is IR active , for example Si[9]. The phonon properties of crystal can be explained to a large extent by the adapted classical Lorentz model:

$$\epsilon_r(\omega) = \epsilon_\infty + (\epsilon_{st} - \epsilon_\infty)\frac{\Omega_{TO}^2}{(\Omega_{TO}^2 - \omega^2 - i\gamma\omega)} \tag{5.1}$$

Where ϵ_r is the relative dielectric constant. The static dielectric constatnt $\epsilon_{st} = 1 + \chi + +\frac{Nq^2}{\epsilon_0\mu\Omega_{TO}^2}$, where μ is the reduced mass, Ω_{TO} is the natural frequency of the optical phonon mode and γ is the damping rate. The high-frequency dielectric constant $\epsilon_0 = 1 + \chi$.

In a lightly damped system, by assuming $\gamma = 0$, we can get a solution of equation 5.1 for $\epsilon_r = 0$ as $\omega = \Omega_{LO}$. Since $\epsilon_r = 0$ indicates longitudinal solution of Maxwell's equations, so $\omega = \Omega_{LO}$ is the frequency of longitudinal mode. By replacing ω with Ω_{LO}, we get the *Lyddane-Sachs-Teller (LST) relationship*:

$$\frac{\Omega_{LO}^2}{\Omega_{TO}^2} = \frac{\epsilon_{st}}{\epsilon_\infty} \tag{5.2}$$

LST relationship implies the degeneracy of TO and LO phonon modes in purely covalent crystals since $\epsilon_{st} = \epsilon_\infty$ when there is no IR active mode.

The reflectivity for a polar crystal can be calculated by using the relative electric permittivity from equation 5.1:

$$R = |\frac{\tilde{n} - 1}{\tilde{n} + 1}|^2 = |\frac{\sqrt{\epsilon_r} - 1}{\sqrt{\epsilon_r} + 1}|^2 \tag{5.3}$$

Because the value of $\sqrt{\epsilon_r}$ is imaginary between Ω_{TO} and Ω_{LO} with $\gamma = 0$, the reflectivity in this region named *Reststrahl band* is 100%. But in real crystal, the reflectivity is relative lower in the Reststrahl band since the damping rate $\gamma \neq 0$.

5.2 Raman scattering

Raman spectroscopy is an ubiquitous method in spectroscopy, biophysics, chemistry and microscopy by studying the inelastic scattering of the monochromatic light. In contrast to IR spectroscopy, Raman spectroscopy is less sensitive due to the weak inelastic scattering process in materials. But Raman spectroscopy has the advantage to freely choose the incident light wavelength, which can avoid the strong absorption of the samples or the environment. Raman spectroscopy is also considered as a complementary method for IR spectroscopy from the perspective of symmetry, because crystals with inversion center obey mutual exclusion rule, which means that any optical mode in the crystal can not be both IR and Raman active at the same time.

Raman scattering arises from the radiation of the electric dipole in a system induced by the electric field of the EM wave. The induced dipole moment in the system can be written as:

$$p = \boldsymbol{\alpha} \cdot \boldsymbol{E} \tag{5.4}$$

Where $\boldsymbol{\alpha}$ is the polarizability tensor. Generally speaking, the polarization of a crystal is the function of the instantaneous positions of the atoms. Hence we can expand $\boldsymbol{\alpha}$ in a series of the normal coordinates:

$$\boldsymbol{\alpha} = \boldsymbol{\alpha}_0 + \sum_k (\frac{\partial \boldsymbol{\alpha}}{\partial Q_k})Q_k + \frac{1}{2}\sum_{k,k'}(\frac{\partial^2 \boldsymbol{\alpha}}{\partial Q_k \partial Q_{k'}})Q_k Q_{k'} + ... \tag{5.5}$$

Where $Q'_k s$ are the normal coordinates of the crystal, and Q_k corresponding to the first order Raman scattering, $Q_k Q'_k$ corresponding to the second order scattering and so on. Usually speaking, first order Raman scattering will dominate the process, but in centrosymmetric materials the second order dominates since the first order Raman scattering is forbidden by the inversion symmetry. Thus hyper Raman starts to play the rule in centrosymmetric materials. By plugging in the lattice wave equation:

$$Q_k = A_k e^{\pm i(\mathbf{k}_k \cdot \mathbf{r} - \omega_k t)} \tag{5.6}$$

into the first order of equation 5.5, and with the incident EM wave $E = E^0 e^{-2i\pi(\boldsymbol{k_E} \cdot \boldsymbol{r} - \nu_E t)}$, we get the first order Raman effect:

$$\boldsymbol{m'} = \boldsymbol{\alpha}_0 E^0 e^{-2i\pi(\boldsymbol{k_E} \cdot \boldsymbol{r} - \nu_E t)} + \sum_k (\frac{\partial \boldsymbol{\alpha}}{\partial Q_k})_0 A_k E^0 e^{2i\pi[(\boldsymbol{k_E} \pm \boldsymbol{k_k}) \cdot \boldsymbol{r} - (\nu_E \mp \nu_k)t]} \tag{5.7}$$

Where the scattered light with frequency $\nu_E \mp \nu_k$ propagates in direction $\boldsymbol{k_E} \pm \boldsymbol{k_k}$. The frequencies given by $\nu_E \mp \nu_k$ are called Stokes and anti-Stokes Raman scattering. When ν_k corresponds to the optical branch of the crystal phonon mode, it is Raman scattering, when it corresponds to the acoustical phonon mode, it is Brillouin scattering.

5.3 Brilloin scattering

Brilloin scattering refers to inelastic light scattering from acoustic phonon mode. The frequency shif the Brilloin scattering is described by equation:

$$\delta\omega = v_s \frac{2n\omega}{c} sin\frac{\theta}{2} \tag{5.8}$$

Where ω is the angular frequency of incident light, v_s is the speed of sound, n is the refractive index, c is the speed of light, and θ is the scattering angle. In Brilloin scattering experiment, single-mode laser and Fabry-Perot interferometer are used in order to detect smaller frequency shift than Raman scattering.

Chapter 6

Optical activity

Certain substances are found to possess the ability to rotate the plane of polarization of light passing through them. This phenomenon is known as *optical activity*. Different from the rotation introduced by birefringence, the rotation angle introduced by optical activity is independent of the incident polarization directions. Optical activity from chiral structural materials are usually called *natrual optical activity* , when people talk about optical activity, usually people refer to natural optical activity, but sometimes the magneto-optical effect or Faraday effect is also included in the phenomena of optical activity. The normal modes of optical active materials are circularly polarized waves. The right- and left-circular-polarization phases experience n_R and n_L two different refraction indexes which introduce the rotation. The rotation angle of the linearly polarized light in optical active materials is proportional to the length of the path of the light through the medium. The amount of rotation per unit length of travel is called the *specific rotatory power*, defined as

$$\delta = \frac{\pi}{\lambda_0}(n_R - n_L) \tag{6.1}$$

where λ_0 is the wavelength of the incident light in vacuum. The plane of polarization rotates towards the circular polarization direction of light with relatively smaller refractive index.

6.1 Magneto-optical effect

When an isotropic dielectric material is placed in a magnetic field and a beam of linearly polarized light transmits through, the plane of polarization of light rotates. This field induced optical activity is *Faraday effect*[10]. The rotation angle θ is proportional to the magnetic induction B and to the length l of the material that the light passed through. Thus we can write:

$$\theta = VBl \tag{6.2}$$

where V is the *Verdet constant*.

To understand Faraday effect, we can start with the motion of a bound electron under external magnetic field $\boldsymbol{B}$ driven by a sinusoidal EM wave $E = E^0 e^{-i\omega t}$, then the equation of motion can be written as:

$$m\frac{d^2\mathbf{r}}{dt^2} + K\mathbf{r} = -e\mathbf{E} - e(\frac{d\mathbf{r}}{dt}) \times \mathbf{B} \tag{6.3}$$

By plugging in the EM wave equation and considering the displacement r with the same harmonic dependence, one can get:

$$-m\omega^2 + K\mathbf{r} = -e\mathbf{E} + i\omega e\mathbf{r} \times \mathbf{B} \tag{6.4}$$

since $\mathbf{P} = -Ne\mathbf{r}$, hence the above equation implies that

$$(-m\omega^2 + K)\mathbf{P} = Ne^2\mathbf{E} + i\omega e\mathbf{P} \times \mathbf{B} \tag{6.5}$$

By solving the three scalor equations, we get the solution:

$$\mathbf{P} = \epsilon_0 \chi \mathbf{E} \tag{6.6}$$

where χ is the susceptibility tensor. Assuming $\mathbf{B}$ is in z direction, we have

$$\chi = \begin{bmatrix} \chi_{11} & +i\chi_{12} & 0 \\ -i\chi_{12} & \chi_{11} & 0 \\ 0 & 0 & \chi_{33} \end{bmatrix} \qquad (6.7)$$

where

$$\chi_{11} = \frac{Ne^2}{m\epsilon_0}\left[\frac{\omega_0^2 - \omega^2}{(\omega_0^2 - \omega^2)^2 - \omega^2\omega_c^2}\right] \qquad (6.8)$$

$$\chi_{33} = \frac{Ne^2}{m\epsilon_0}\left[\frac{1}{\omega_0^2 - \omega^2}\right] \qquad (6.9)$$

$$\chi_{11} = \frac{Ne^2}{m\epsilon_0}\left[\frac{\omega\omega_c}{(\omega_0^2 - \omega^2)^2 - \omega^2\omega_c^2}\right] \qquad (6.10)$$

In which, the $\omega_0 = \sqrt{\frac{K}{m}}$ is the resonance frequency, and $\omega_c = \frac{eB}{m}$ is the cyclotron frequency.

Faraday effect is one of the earliest demonstration of the interaction between light and magnetism and it has broadly practical applications. It can be used to analyse the constituents of hydrocarbons, since each constituent has a characteristic magnetic rotation. Faraday effect can also be used in optical modulators and optical isolators.

6.2 Natural optical activity

It is not surprise to see that the susceptibility tensor for natural optical activity is in the same form with the one for Faraday effect, equation 6.7. The refractive index for right and left circularly polarized light is written as:

$$n_R = \sqrt{1 + \chi_{11} + \chi_{12}}$$
$$n_L = \sqrt{1 + \chi_{11} - \chi_{12}} \qquad (6.11)$$

According to the equation 6.1, the rotation power for optical active material is:

$$\delta = \frac{\pi}{\lambda_0}(n_R - n_L) \approx \frac{\pi}{\lambda_0}\frac{\chi_{12}}{\sqrt{1+\chi_{11}}} = \frac{\chi_{12}\pi}{n_o\lambda_0} \tag{6.12}$$

Where n_o is the ordinary index of refraction. This result shows that the rotation power of natural optical activity is directly related to the imaginary component of χ_{12} in the susceptibility tensor.

Natural optical activity can be found in organic liquid such as turpentine, as well as solutions of camphor and sugar, which have chiral molecules. It can aslo be found in crystals such as quartz, and $BaCoSiO_4$ as demonstrated in our following experiment result , which have chiral crystal structures. In contrast to the Faraday effect, the origin of natural optical activity is more sophisticated and it can be understood from spatial dispersion[11] or electromagnetic inductions of materials with chiral structures[12, 13].

6.3   Magneto-chiral effect

Magnetochiral dichroism (MChD) appears as a difference in the absorption coefficient of chiral systems for unpolarized light beams propagating parallel and antiparallel to a external magnetic field[14, 15]. MChD effect is a key to realize artificial gauge field for light[16], and it is also possible to realize one-way mirrors due to the directional birefringence of unpolarized light.

Based on the aforementioned effect, the refractive index of the medium with magnetism and chirality is written as[12]:

$$n_t^{\pm} = \sqrt{\epsilon\mu} \pm \frac{1}{4}\sqrt{\frac{\epsilon}{\mu}}\kappa \pm \frac{\xi sgn(k_t)}{2} + \frac{1}{4}\xi sgn(k_t)\frac{\kappa}{\mu} \tag{6.13}$$

Where the first term on the right-hand side is conventional dispersion without symmetry breaking. The second term is proportional to the external magnetic field that breaks the time reversal symmetry, which represents the MO effect, and depends on polarization states. The forth term breaks the space-inversion symmetry and represents the OA by the chirality tensor ξ. The last term is a mixture of chirality and external magnetic field, and it represents the Mch effect. This term simultaneously break the space-inversion and time-reversal

symmetries, it is independent of the polarization state because ξ and κ both depend on the polarization state and they cancel out.

Chapter 7

Symmetry, order and non-reciprocity

The spaciotemporal symmetries are closely related to the properties of crystals in various aspects, for instance, multiferroics, Weyl semimetals,ferromagnetic materials, chiral materials, quantum spin liquid, Faraday effect, optical second harmonic generation, optical activity, photogalvanic effect are all defined with certain symmetry breaking. A symmetry is global if the Hamiltonian of the system is invariant by applying the symmetry operation on the entire system. A symmetry is local if the Hamiltonian is invariant by applying the symmetry operation differently to different points.

All symmetry operations in crystals are discrete.The discrete symmetry operations include: translational symmetry, rotational symmetry, mirror reflection symmetry, space inversion symmetry and time reversal symmetry.

Many physical quantities in condensed matter physics can be distinguished by their symmetries, the categorization of vectorlike physical quantities by space-time rotation group $O(3) \times \{1, 1'\} = O'(3)$ is shown in table 7.1, where $O(3)$ is the group of proper and improper rotations and $1'$ is the time reversal operation.

In the symbol column of the table 7.1, **G** is for time-even axial vector, for example: electric toroidal moment, **P** is for time-even polar vector, for example: polarization, **M** is for time-odd axial vector, for example: magnetization, **T** is for time-odd polar vector, for example: magnetic toroidal moment or Poynting vector, **N** is for time-even neutral vector, for example: rodlike molecules in nematic phases of liquid crystal, **C** is for time-even chiral vector, for example:

TABLE 7.1: One-dimensional irreps character table for the eight types of vectorlike physical quantities. The extra dash symbol identifies the operation with time reversal symmetry, and the 'm' infront of the irrep label indicates antisymmetry with respect to time reversal. [17]

Irrep	E ∞ $2_{\parallel}$	$\bar{1}$ $\overline{\infty}$ $m_{\perp}$	$m_{\parallel}$	$2_{\perp}$	$1'$ ∞' $2'_{\parallel}$	$\bar{1}'$ $\overline{\infty}'$ $m'_{\perp}$	$m'_{\parallel}$	$2'_{\perp}$	Symbol
$A_{1g}(\Sigma_g^+)$	1	1	1	1	1	1	1	1	**N**
$A_{2g}(\Sigma_g^-)$	1	1	−1	−1	1	1	−1	−1	**G**
$A_{1u}(\Sigma_u^+)$	1	−1	1	−1	1	−1	1	−1	**P**
$A_{2u}(\Sigma_u^-)$	1	−1	−1	1	1	−1	−1	1	**C**
$mA_{1g}(m\Sigma_g^+)$	1	1	1	1	−1	−1	−1	−1	**L**
$mA_{2g}(m\Sigma_g^-)$	1	1	−1	−1	−1	−1	1	1	**M**
$mA_{1u}(m\Sigma_u^+)$	1	−1	1	−1	−1	1	−1	1	**T**
$mA_{2u}(m\Sigma_u^-)$	1	−1	−1	1	−1	1	1	−1	**F**

helix, **L** is for time-odd neutral vector and **F** represents time-odd chiral vector, for example: the 'false chirality'.

7.1 Landau theory of phase transition

The phenomena of spontaneous order or spontaneous symmetry breaking at critical temperature T_c is fundamentally important in condensed matter physics. Material undergoes a phase transition due to spontaneous symmetry breaking and this phenomenon can be characterized by an order parameter η which is often zero above T_c and non-zero below. In Landau theory, the free energy functional can be expanded as a series function of even power of the order parameter if the system possess certain symmetries:

$$F(T, \eta) - F_0 = a(T)\eta^2 + \frac{b(T)}{2}\eta^4 + ... \tag{7.1}$$

In general, it is a good approximation to consider the series to the forth power, the coefficient $b(T)$ is taken as a positive constant b_0 if the system is thermaldynamically stable, the coefficient $a(T)$ is expanded to the first order $a(T) \approx a_0(T - T_c)$ with $a_0 > 0$ and will change sign at the critical temperature T_c. The

free energy vs. order parameter is plotted in figure 7.1 a under different temperatures, above T_c the order parameter is zero, while below T_c there are two solutions for η. As the temperature T gradually decrease from high to T_c, one can see immediately that the free energy gets shallower, the shallow dependence of the lattice free energy causes the long-lived birefringent state in $KTaO_3$ which will be introduced in the following section.

By minimizing the free energy, one can find two solutions:

$$\eta = \begin{cases} 0 & T > T_c \\ \\ \sqrt{-\frac{a_0}{b_0}(T - T_c)} & T < T_c \end{cases} \tag{7.2}$$

The solutions is plotted in figure 7.1 b, with the temperature above T_c, the order parameter is zero and non-zero below T_c.
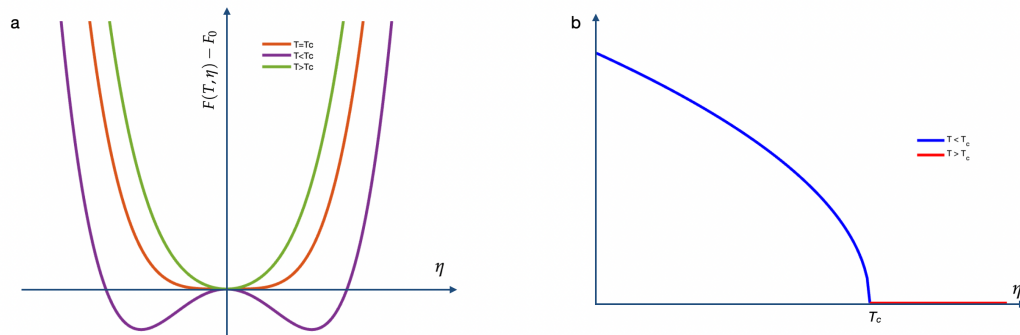
FIGURE 7.1: (a) Temperature dependence of free energy vs. order parameter. (b) Temperature dependence of order parameter.

7.2 Optical non-reciprocity

Non-reciprocity phenomena are ubiquitous in nature, for example, electric diode or p-n junction which is broadly used in electronic engineering, the inbuilt **E** field breaks the inversion symmetry of the device which introduces the different behaviors of the counterpropagating electrons. Similarly, the crystals with optical non-reciprocity are those which can distinguish the emerged conterpropagating light beams irrespective of the polarization state of the light[14].

Under this definition, the Faraday effect is not considered as an example of optical non-reciprocity, because it is non-reciprocal for circularly or elliptically polarized light, but reciprocal for linearly polarized light.

The difference of counterpropagating light beams can exhibit in forms of rotation power, absorption coefficient, reflectivity and so on. One example in THz domain is the hight-temperature THz dichroism in polar ferrimagnet $FeZnMo_3O_8$, the configurations of the toroidal moment $\mathbf{T} = \mathbf{P} \times \mathbf{M}$ parallel and antiparallel with the propagation direction of the THz light beam introduce giant difference in absorption coefficients[18], this phenomenon is termed *optical magnetoelectric effect*. Another interesting example of optical non-reciprocity is *magneto-chiral dichroism*, different absorption coefficients are observed for THz lgith beam travel parallel and antiparallel with the external $\mathbf{B}$ field in a chiral material $Ba_2CoGe_2O_7$[19].

7.3 Symmetry-operational similarity

This section focus on the understanding of Symmetry-operational similarity (SOS) in the application of optical non-reciprocity in complex materials. SOS analysis is an empirical result proposed that the optical non-reciprocity can occur when the specimen constituents and measuring probes share SOS in the relation of broken symmetries[20, 21].
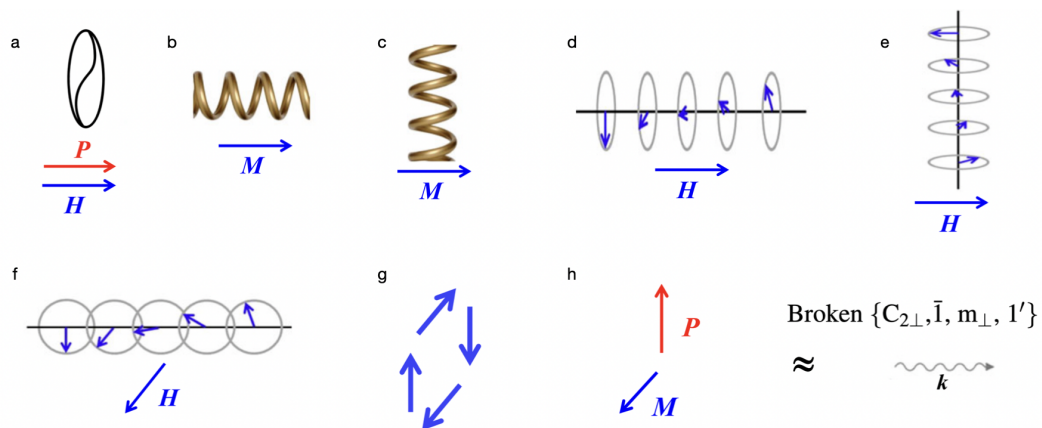
FIGURE 7.2: (a) Ferro-rotation. (b)(c) Structural chirality. (d)(e) Helical spin order. (f) Cycloidal-spin order. (g) Toroidal moment of rotating spins. (h) Toroidal moment with **P** and **M**. [21]

Optical beam can be characterized by wave vector $\mathbf{k}$, which breaks the symmetry operations $\{C_{2\perp}, \bar{1}, m_\perp, 1'\}$, here $'\perp'$ represents the operation that is perpendicular to the $\mathbf{k}$ vector. Figure 7.2 lists the specimen configurations that break the same set of symmetry operations with $\mathbf{k}$ vector, which are predicted to exhibit optical non-reciprocity from the perspective of SOS.

Here we analyse two configurations which are closely related to our following experiments as examples. Figure 7.2(b) shows a chiral crystal structure with magnetization along the chiral axis. The spiral structure breaks $\bar{1}$, $m_\perp$ symmetries, and the magnetization breaks $C_{2\perp}$ and $1'$ symmetries, so compare with the set of broken symmetries from $\mathbf{k}$ vectors, we know this configuration satisfies SOS condition. For figure 7.2 (h), we know that the polarization $\mathbf{P}$ breaks the $\bar{1}$, $m_\perp$ symmetries, and the magnetization breaks $C_{2\perp}$ and $1'$ symmetries, so the SOS condition is also satisfied.

Chapter 8

Magnetic materials

Along with the utilization of electricity and wireless communication, magnetism has played an important role in modern industry. In this section, we focus on the magnetic interactions in crystals, introduce the basic concepts based on the textbooks[22, 23], and summarize the ideas of geometric frustration and quantum spin liquid which closely related to our following research.

8.1   Magnetic moment and interactions

Electron has intrinsic angular momentum (spin) with half-integer spin quantum number $s = \hbar/2$ and the observable projections $s_z = \pm\hbar/2$. The magnetic moment of an electron due to spin is given by:

$$\mu_z = -\mu_B \tag{8.1}$$

Where $\mu_B = \frac{e\hbar}{2m_e}$ is the *Bohr magneton*. From equation 8.1 we know that the electron magnetic moment is antiparallel with its spin direction.

The energy of a magnetic moment μ in a magnetic field **B** is given by:

$$E = -\boldsymbol{\mu} \cdot \mathbf{B} \tag{8.2}$$

So the energy is minimized when the magnetic moment is parallel with the **B** field. However, since the magnetic moment is associated with spin angular momentum, μ instead of turning towards **B**, it precess around the magnetic field **B**:

$$\frac{d\mu}{dt} = \gamma\mu \times \mathbf{B} \tag{8.3}$$

With the Larmor precession frequency $\omega_L = \gamma B$.

Magnetic interaction is a key element for magnetic materials. Magnetic dipolar interaction is maybe the first interaction one expects to play a role in magnetism. The energy of two magnetic moment μ_1 and μ_2 separated by distance r is:

$$E = \frac{\mu_0}{4\pi r^3}[\mu_1 \cdot \mu_2 - \frac{3}{r^2}(\mu_1 \cdot r)(\mu_2 \cdot r)] \tag{8.4}$$

The energy magnitude for two electrons separated by distance $r \approx 1\mathring{A}$ is estimated to be $10^{-23}J$, which is equivalent to about $1K$ in temperature. So it turns out that the magnetic dipolar interaction is too weak to be significant in magnetic materials at high temperature, other magnetic interaction mechanisms must be considered.

8.1.1 Exchange interaction

Exchange interaction lies in the center of the magnetic long range ordering. It is nothing more than electrostatic interactions, the interaction energy increases when electrons are close together and decreases when they are apart. The spin-dependent effective Hamiltonian for all neighbouring atoms can be written as:

$$\hat{H} = -\sum_{ij} J_{ij}\mathbf{S_i} \cdot \mathbf{S_j} \tag{8.5}$$

If $J > 0$, the triplet state is favored, for example, two electrons on the same atom, the triplet state ensures an antisymmetric spatial state to separate the electrons apart to save potential energy. While for $J < 0$, the singlet state is favored,

for example, two electrons on neighbouring atoms, the singlet state ensures an symmetric bonding state to save kinetic energy.

Electrons on neighboring magnetic atoms interact via an exchange interaction directly is called *direct exchange*. Usually, direct exchange is not the main mechanism of magnetic properties of materials due to the insufficient direct overlap of neighboring magnetic orbitals. Here in the following sections, we discuss a couple of different indirect exchange interactions which is more significant in magnetic materials.

8.1.2 Superexchange interaction

The indirect exchange interaction between two non-neighbouring magnetic ions mediated by a non-magnetic ion in between is termed *superexchange interaction*. Figure 8.1 shows two transition metal ions mediated by a oxygen ion, antiferromagnetic coupling is favored because it allows the delocalized electrons to move over the whole structure. In most cases, antiferromagnetic configuration is favored by superexchange interactions, but in some particular circumstances, ferromagnetic configuration is possible.
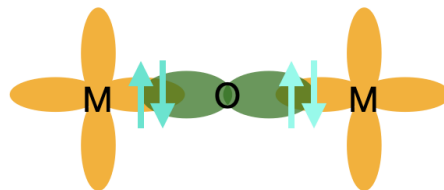
FIGURE 8.1: Superexchange interaction

8.1.3 Double exchange interaction

In some oxides, it is possible to have a ferromagnetic exchange interaction which occurs because the magnetic ion can show mixed valency, this mechanism is called *double exchange*. Double exchange interaction favors the ferromagnetic alignment as shown in figure 8.2 with Mn^{3+} and Mn^{4+} as an example. The e_g

electrons can only hop to the the neighbor ion freely with the high spin configuration and thus lowers the kinetic energy. Because of the itinerant properties of the e_g electrons, these materials become metallic.
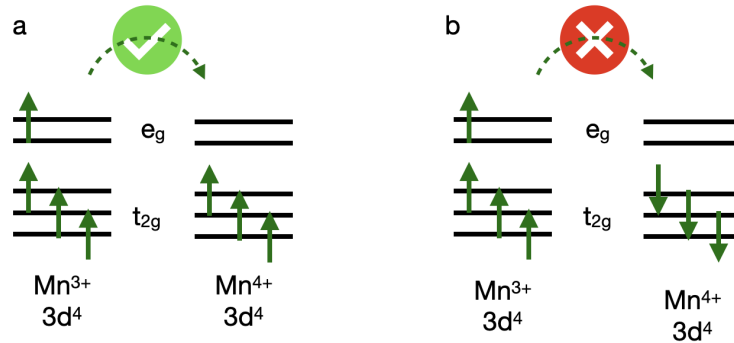
FIGURE 8.2: Double exchange interaction. (a) Neighbouring ions are ferromagnetically aligned, the e_g electron is allowed to hop to the neighbor. (b) Neighbouring ions are antiferromagnetically aligned, so the e_g electrons cannot hop to the neighbor freely.

8.1.4 Dzyaloshinsky-Moriya interaction

The *anisotropic exchange interaction* is also termed as *Dzyaloshinsky-Moriya interaction (DMI)*, it describes the interaction between the excited state of one ion with the ground state of the other through spin-orbit interaction in a noncentrosymmetric configuration. The Hamiltonian of DMI can be written as:

$$\hat{H}_{DM} = \boldsymbol{D} \cdot (\boldsymbol{S_1} \times \boldsymbol{S_2}) \tag{8.6}$$

Where vector $\boldsymbol{D}$ vanishes when the crystal field has inversion center at the oxygen ion. When the oxygen ion is off the inversion center, a polarization $\boldsymbol{P}$ formed between the transition metal and oxygen ions as shown in figure 8.3. The polarization $\boldsymbol{P}$ is expressed as:

$$\boldsymbol{P} \propto \sum_{ij} \boldsymbol{e_{ij}} \times (\boldsymbol{S_1} \times \boldsymbol{S_2}) \tag{8.7}$$

Here $\boldsymbol{e_{ij}}$ is the vector connecting the two transition metal ions. This mechanism is the origin of the polarization $\boldsymbol{P}$ in cycloidal structure.
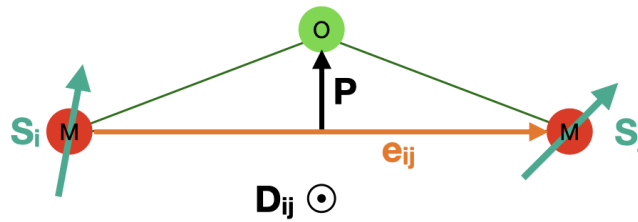
FIGURE 8.3: Anisotropic exchange interaction. .

8.2 Crystal field theory

The crystal field of magnetic materials is an electric field derived from neigh-bouring atoms in the crystal. From the section of magnetic interactions, we learned that the environment of magnetic ions is significant for the properties of magnetic materials, since the crystal field and d orbit electron density of mag-netic irons are usually not spherical, the interactions exhibit pronounced angu-lar dependence.

Take the octahedral environment as an example, the magnetic ion is surrounded by six oxygen ions. The degeneracy of d orbitals of the magnetic ion is lifted by the crystal field into two categories: e_g orbitals ($d_{z^2}, d_{x^2-y^2}$)and t_{2g} orbitals (d_{xy}, d_{xz}, d_{yz}), figure 8.4. From figure 8.4(d)(e) one can learn that the e_g orbital $d_{x^2+y^2}$ has larger overlap with the p orbitals of the oxygen ions than the d_{xy} orbital in t_{2g}, thus d_{xy} orbital energy is lowered while the $d_{x^2+y^2}$ orbital energy is raised. Interestingly, the crystal field works exactly in the opposite sense in the tetrahedral environment.

8.3 Categorization of magnetic materials

According to the different behaviors of the magnetic susceptibility χ and Curie temperature T_c, one can classify magnetic materials into diamagnetic materials, paramagnetic materials, ferromagnetic materials, antiferromagnetic materials and ferrimagnetic materials.

For the diamagnetic materials, $\chi < 0$. Diamagnetism arises from the interac-tion of the external field B with orbital magnetic moment of electrons. Strictly
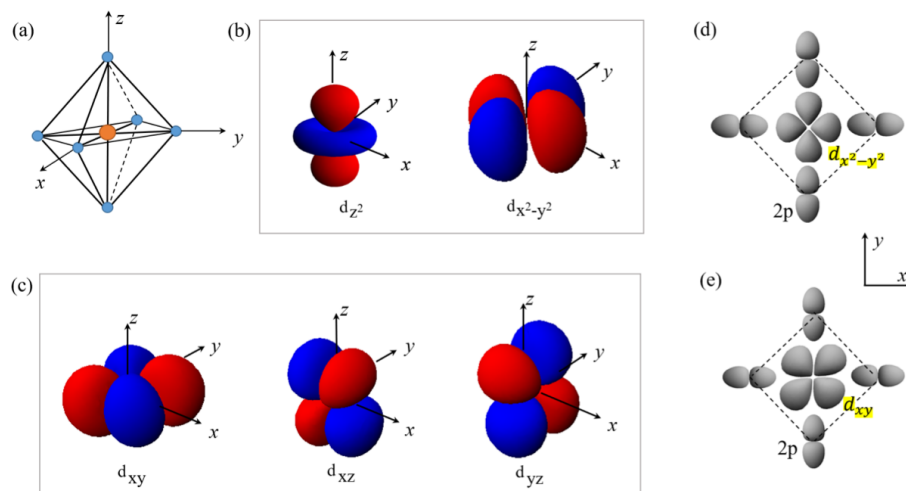
FIGURE 8.4: (a) A 3d metal ion at the center of an octohedron formed by oxygen ions. (b)(c) Probability distributions of e_g orbitals and t_{2g} orbitals, respectively. (d)(e) Orbiatal overlaps between the oxygen $2p$ orbitals and $d_{x^2-y^2}$ and d_{xy} orbitals, respectively.[24]

speaking, all materials have diamagnetism, but usually diamagnetism is insignificant unless the the ions in materials have completely filled orbitals.
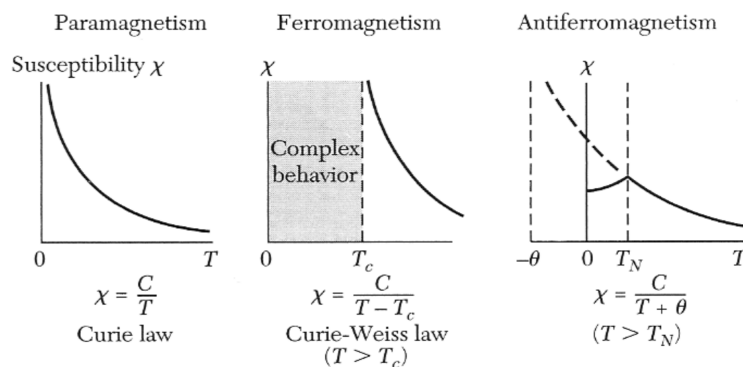
FIGURE 8.5: Curie Weiss law for different magnetic materials. [25]

For magnetic materials with susceptibility $\chi > 0$, based on the *Curie Weiss law*, if $T_c = 0$, it is paramagnetic material, if $T_c > 0$, it is ferromagnetic material, if $T_N < 0$ and spins in two sublattices are equal in magnitude, it is antiferromagnetic material, and if the spins in sublattices have unequal magnetic moments, it is ferrimagnetic materials. The categorization is summarized in figure 8.5.

8.4   Magnetic resonance

When a magnetic material is exposed in an external $\boldsymbol{B}$ field, from equation 8.3 one knows that instead of turning towards the magnetic field, the magnetic moment $\boldsymbol{\mu}$ precesses around it with a frequency $\omega_L = \gamma B$. The energy of the system is quantized into discrete levels due to the quantization of the orbital angular momentum. An external EM wave with corresponding frequency can be absorbed by the system and drives the system to an excited state, this process is called *magnetic resonance*. Different magnetic resonance techniques involve different EM frequency ranges, here we discuss nuclear magnetic resonance and ferromagnetic resonance which corresponding to the frequency ranges MHz and GHz, respectively.

8.4.1   Nuclear magnetic resonance

Nuclear magnetic resonance (NMR) is the magnetic resonance of EM wave with the magnetic moment of nuclears. This technique is broadly used in medical imaging, but it is also very helpful for us to further understand the electron spin magnetic resonance in magnetic materials and other resonant phenomena in the study of condensed matter physics. For a proton, $I = 1/2$ and m_I can only take the values of $\pm 1/2$, the corresponding energy splitting under $B = 1T$ is $\sim 10^{-7} eV$, the equivalent temperature is $\sim 1mK$, and the equivalent frequency is $42.58 MHz$, which is in the radiofrequency region.

The absorption rate of the EM wave of a two level system through NMR is described by equation:

$$\frac{dE}{dt} = -W\hbar\omega n(t) \tag{8.8}$$

Where E represents the energy of the system, W is the transition rate and $n(t)$ is the population difference between the excited state and the ground state.

The most interesting phenomena of NMR we want to discuss here is the relaxation time. In NMR measurement, there are two distinct relaxation time T_1 and T_2. T_1 originates from the interaction of the field induced magnetization in z direction with the lattice vibrations, and this process is accompanied with energy

transfer. While T_2 characterizes the dephasing time of the interaction between different parts of the spin system in the xy plane, this process has no energy consequences because the applied field is along z direction. The relaxation behavior of NMR is:

$$\frac{dM_x}{dt} = \gamma(\boldsymbol{M} \times \boldsymbol{B})_x - \frac{M_x}{T_2}$$
$$\frac{dM_y}{dt} = \gamma(\boldsymbol{M} \times \boldsymbol{B})_y - \frac{M_y}{T_2} \qquad (8.9)$$
$$\frac{dM_z}{dt} = \gamma(\boldsymbol{M} \times \boldsymbol{B})_z - \frac{M_0 - M_z}{T_1}$$

8.4.2 Ferromagnetic resonance

For an isolated electron with spin$-1/2$, under an external magnetic field $B = 1T$, and taking $g_e \approx 2$, one can get the spin resonance frequency readily about $28GHz$, which is close to the the THz range $(0.1 - 30THz)$.

Charles Kittel gave a solution for ferromagnetic resonance half century ago[26] which resolved the Larmor Frequency anomaly in Griffiths paper[27]. He started from equation $\frac{\partial \boldsymbol{J}}{\partial t} = \boldsymbol{M} \times \boldsymbol{H}$, where $\boldsymbol{J}$ is the angular momentum density and $\boldsymbol{M}$ is the magnetization. By plugging in $\boldsymbol{J} = 1/\gamma \boldsymbol{J}$, one gets the equation:

$$\frac{\partial \boldsymbol{M}}{\partial t} = \gamma[\boldsymbol{M} \times \boldsymbol{H}] \qquad (8.10)$$

Where the components of $\boldsymbol{H}$ are $(H_x, -4\pi M_y, H_z)$. Here the H_y component is replaced by $-4\pi M_y$ based on the divergence relation $B_y = H_y + 4\pi M_y = 0$. By plugging $\boldsymbol{H}$ in equation 8.10 and neglecting the small quantities, one gets:

$$\frac{\partial M_x}{\partial t} = \gamma(M_y H_z + 4\pi M_y M_z) = \gamma B_z M_y$$
$$\frac{\partial M_y}{t} = \gamma(M_z H_x - M_x H_z) \qquad (8.11)$$
$$\frac{\partial M_z}{\partial t} = 0$$

By solving these equations, one can get the resonant frequency $\omega_0 = \gamma(B_z Hz)^{1/2}$.

Chapter 9

Terahertz spectroscopy

9.1 Back ground

Terahertz (THz) radiation refers to a frequency band, it is also called 'T-ray'. The spectrum region lies between microwave and infrared region. THz band has enormous spectral features associated with many fundamental physical processes such as molecular rotations, lattice vibrations, intraband transitions, superconducting gap and so on. The frequently used units corresponding to 1 THz are as following:

(1) Frequency: $v = 1 THz = 1000 GHz$

(2) Period: $\tau = 1/v = 1 ps$

(3) Wavelength: $\lambda = c/v = 0.3 mm = 300 \mu m$

(4) Wavenumber: $\bar{k} = k/2\pi = 1/\lambda = 33.3 cm^{-1}$

(5) Photon energy: $hv = \hbar\omega = 4.14 meV$

(6) Temperature: $T = hv/k_B = 48 K$

9.2 Experiment setups

Figure 9.1 shows the schematic diagram for THz time domain spectroscopy by using optical rectification and free space electro-optic sampling as generating
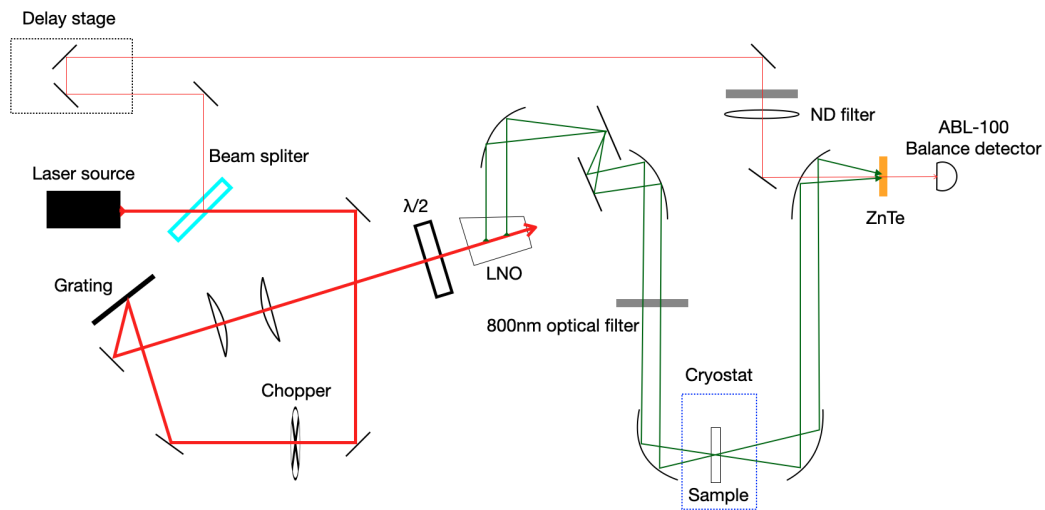
FIGURE 9.1: THz time domain spectroscopy.

and detecting methods, these methods can be easily replaced by photoconductive antenna. By adding a polarizer before the receiver to measure $\pm 45°$ transmitted THz amplitude, we can easily calculate the rotation angle and ellipticity of the tramsmitted THz light. By conducting the sample-reference measurement, we can calculate the complex refractive index of materials as well as other characteristic coefficients such as absorption coefficient α, distinction coefficient k and conductivity σ.
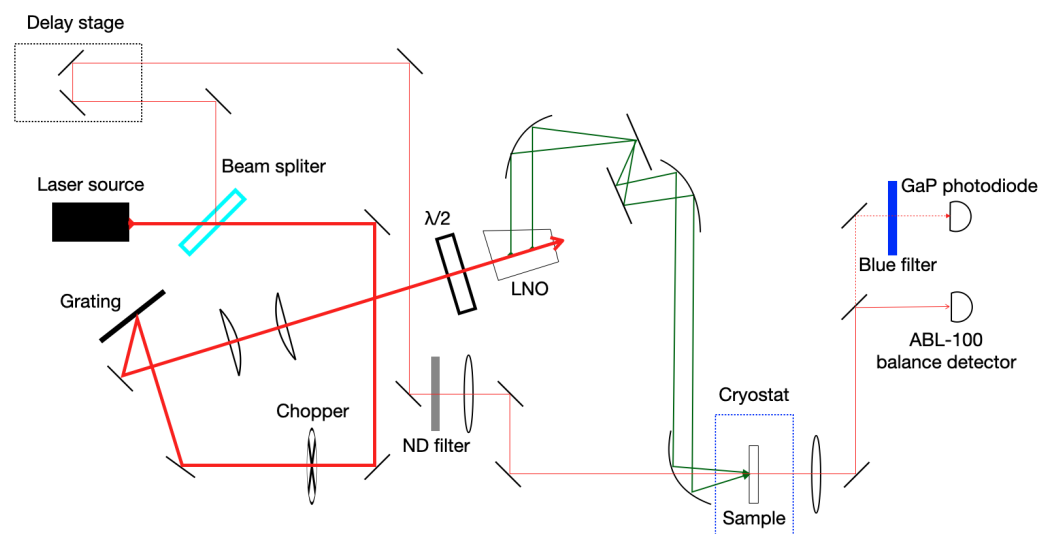
FIGURE 9.2: THz-pump optical-probe spectroscopy.

Figure 9.2 shows the schematic diagram for THz-pump optic-probe spectroscopy.

In this set up, the THz light works as pump to excite materials into higher energy state in picosecond time scale, by using this method, one is allowed to study the ultrafast dynamics of materials. At the receiver end of this schematic diagram, by using GaP (band gap = 2.24eV) photodiode detector accompanied with a blue filter, one can measure the THz *field-induced second harmonic generation (TFISH)* of the fundamental beam. While by using the balance detector as a receiver, one can measure the *THz field-induced Kerr effect (TKE)*. These effects are closely investigated in *$KTaO_3$* in the following experiments.

9.3 THz generation

9.3.1 Femtosecond Laser

THz spectroscopy is performed using a home-built spectrometer based on a 1-kHz repetition rate regenerative Ti:Sapphire laser amplifier. The predominant gain medium Ti:Sapphire has several outstanding properties to produce ulstrashort laser pulses:

(1) The gain spectrum is extremely broad ranging from 650 to 1100 nm.

(2) The crystal has high thermal conductivity and can take upto 20 W optical pumping power.

(3) The carrier lifetime is relatively small, about 3.2 ms.

The generated laser pulse in the lab has 800 nm wave length, 37 fs duration time, and about 4 mJ energy per pulse.

9.3.2 Photoconductive antenna

Photoconductive antenna (PCA) is an electrical switch that can be used both as THz emitter and receiver. In order to have a PCA work in THz domain, the switch-on and off time must be limited in the subpicosecond range. The switch-on time is mainly determined by the laser pulse duration while the the switch-off time depends on the lifetime of the photoexcited carriers. The lifetime of the
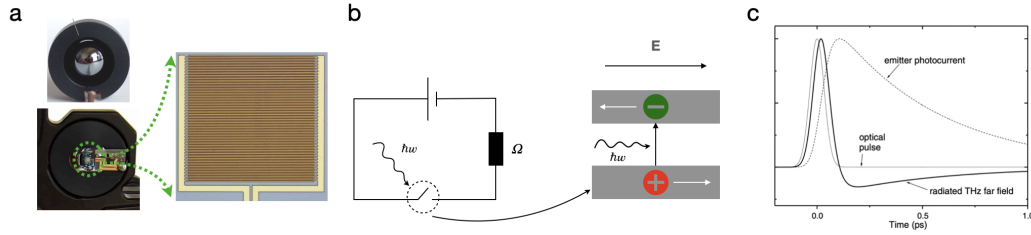
FIGURE 9.3: Schematic diagram for PCA and simulated THz radiation. a. Top view of interdigital PCA (iPCA) with microlens array. b. THz generation in iPCA. c. Bow-tie PCA THz receiver. The THz electric field works as DC field relative to the femtosecond optical pulse. d. The simulated emitter photocurrent and correspongding radiated THz far field[8].

excited carriers is determined by the concentration of the defects in the materials. The commonly used materials for PCA are low-temperature grown gallium arsenide (LT-GaAs) and radiation-damaged silicon-on-sapphire (RD-SOS). The high concentration defects of LT-GaAs are mainly from point defects, such as antisites, while RD-SOS are from O^+ ion implantation in the silicon layer. The typical PCA emitter and detector used in our lab is shown in figure 9.3.

The instantaneous electric field of the emitted THz light from a PCA can be written as:

$$E_{THz}(t) = \frac{\mu_0 \omega_0 sin(\theta)}{4\pi r} \frac{\mathrm{d}I_{PC}(t_r)}{\mathrm{d}t_r} \hat{\theta} \propto \frac{\mathrm{d}I_{PC}(t)}{\mathrm{d}t} \tag{9.1}$$

Which is proportional to the rate of the induced photocurrent in the PCA.

Assuming the incident laser pulse is Gaussian with the duration time $2\sqrt{ln2}\tau_p$, one can derive the photocurrent:

$$I_{pc}(t) = \frac{\sqrt{\pi}}{2}\mu_{(e)}E_{DC}I_{opt}^0[\exp\left(\frac{\tau_p^2}{4\tau_c^2} - \frac{t}{\tau_c}\right) \cdot erfc(\frac{\tau_p}{2\tau_c} - \frac{t}{\tau_p}) -$$
$$\exp\left(\frac{\tau_p^2}{4\tau_{cs}^2} - \frac{t}{\tau_{cs}}\right) \cdot erfc(\frac{\tau_p}{2\tau_{cs}} - \frac{t}{\tau_p})] \tag{9.2}$$

where $erfc(x) = 1 - erf(x) = \frac{2}{\sqrt{\pi}}\int_x^\infty e^{-t^2}\mathrm{d}t$, $\frac{1}{\tau_{cs}} = \frac{1}{\tau_c} + \frac{1}{\tau_s}$, $I_{opt}(t)$ is the intensity profile of the optical pulses, $\mu_e = e\tau_s/m$ is the electron mobility.

9.3.3 Tilted wave-front phase-matching method

Optical rectifictation in noncentrosymmetric materials is another method for THz generation, it has already been established in the chapter of nonlinear optics, so here we only introduce the tilted wave-front phase-matching method as the application of optical rectification.

LiNbO$_3$ (LNO) is a ferroelectric material. Its crystal structure belongs to trigonal crystal system with space group R3c. LNO has high optical transparency from 350-5200 nm. The electro-optic coefficient d$_{33}$ of LNO is 27 pm/V which makes it a perfect material for THz generation[8]. In our setups, we use tilted wave-front phase-matching method in LNO to generate THz. The schematic diagram is shown in figure 9.4. In order to satisfy the phase-matching condition in LNO, we use a grating here to tilt the wave-front of the incident light, the angle θ as shown in figure 9.4 is 64°, and the first order diffraction beam of the grating is chosen as the generating beam, the slits distance of the grating here is 1800 grooves/mm.
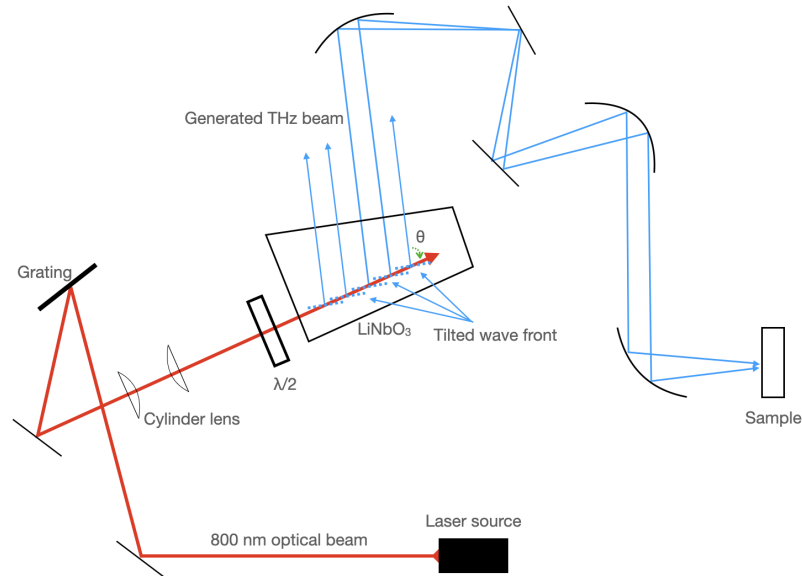
FIGURE 9.4: THz generation by tilted wave-front phase-matching method in LiNbO$_3$ bulk crystal.

The phase matching condition for two waves with frequency ω_1 and ω_2 can be written as:

$$\Delta\Phi = (k^{(\omega_2)} - 2k^{(\omega_1)})l_c = 2\pi \qquad (9.3)$$

where, $l_c = \frac{\lambda}{2[n^{(\omega_2)} - n^{(\omega_1)}]}$ is the coherence length, $n^{(\omega_1)}$ and $n^{(\omega_2)}$ are the refractive indices.

In order to have all the emitted THz light in phase from the LNO crystal, the cutting angle of the crystal relative to the incident laser beam is particularly choose as 64°, which matches the tilting angle of the incident wavefront. The tilting angle is calculated from the refractive indices of the optical beam and the THz beam below:

$$\theta = cos^{-1}(\frac{n_o}{n_T}) \approx 64° \tag{9.4}$$

9.3.4 Spin current injection
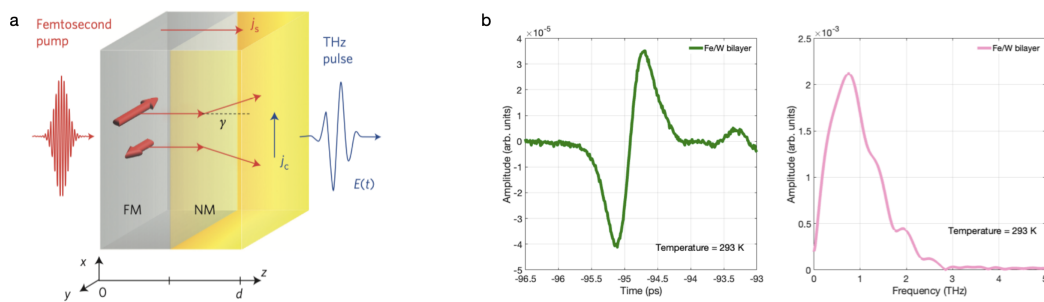
FIGURE 9.5: a. Schematic diagram of the mechanism for spin current injection method[28]. b. THz pulse generated by Fe/W bilayer by using spincurrent injection method in our lab.

THz generation in ultrathin metal bilayer by spincurrent injection is an extremely promising new generation of THz emitter because of its large bandwidth ($1 - 30THz$), large field amplitude at low pump power, scalability and low cost[28, 29].

Figure 9.5 (a) illustrates the basic principle of the spintronic emitter. The device is made of two layers of materials, the first layer is ferromagnetic material (FM) and the second layer is nonferromagnetic material (NM) but with strong spin-obit coupling. By applying an external magnetic field antiparallel with y axis, the spin population along the field direction in the FM layer gets higher than the population in the opposite direction. The femtosecond pump laser excites the electrons in FM layer above the Fermi energy and the excited electrons start to launch along z direction over the interface. Electrons with opposite spins are

scattered by the NM layer in the opposite directions which form the transverse net current in the x direction and generate the THz light. A THz pulse and the corresponding frequency band generated in a Fe/W bilayer synthesized by sputtering method is shown in figure 9.5(b).

This process of a spin current generates transverse net current is called *inverse spin Hall effect* or *Mott scattering*[23, 30]. Mott scattering can be understood from the perspective of the force on a magnetic dipole **m** in a field **H**, equation 9.5, and the field here is created by the relative motion of the nucleus with the electrons in the NM layer.

$$\mathbf{F} = \nabla(\mathbf{m} \cdot \mathbf{H}) = (\mathbf{m} \cdot \nabla)\mathbf{H} \tag{9.5}$$

9.4 THz detection

9.4.1 Photoconductive antenna

The mechanism underlies the PCA receiver is almost identical with the PCA emitter. In this setup, the THz electric field, instead of the external *dc* field, drives the injected electrons. The lifetime of the excited electrons must be in subpicosecond range in order to have time resolution of THz pulse. The induced photocurrent is proportional to the amplitude of the THz electric field. By scanning the optical path of the laser beam, one is allowed to map out the THz waveform.
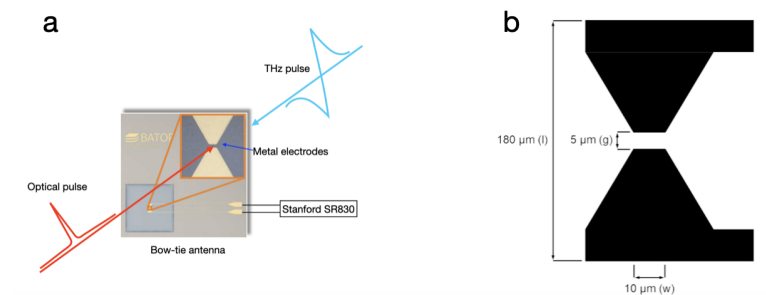
FIGURE 9.6: Bow-tie type THz receiver. (a) The schematic diagram of time resolved THz detection by a bow-tie PCA. (b) A magnified picture of the PCA antenna. .

9.4.2   Free-space electro-optic sampling
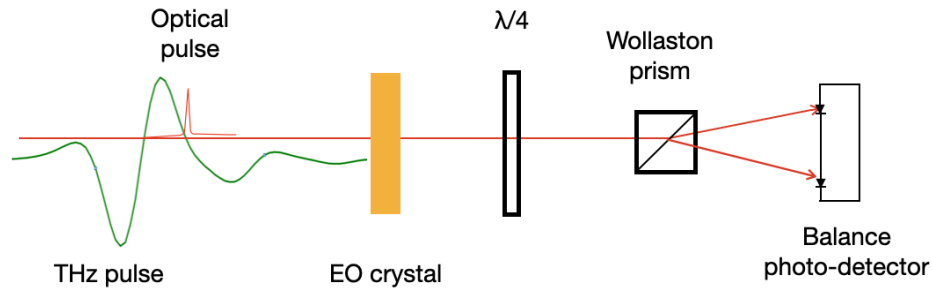
FIGURE 9.7: The schematic diagram for free-space electro-optic sampling.

As an alternative method of THz detection, *free-space electro-optic sampling method* also can measure the amplitude of THz light in time domain as well as the phase with precision$< 10^{-2} rad$. The underlying physics for this method is Pockels effect which has been discussed in the chapter of nonlinear optics. The schematic diagram is shown in figure 9.7. The electric field of the THz light modulates the refractive index of the *EO crystal* and rotates the linearly polarized optical pulse by angle $\Delta\phi$, the quarter wave plate converts the linearly polarized light into elliptically polarized, then the *Wollaston prism* splits it into two linearly polarized light and eventually detected by the *balanced photo-detector* and generates photocurrent I_x and I_y, where $'x'$ and $'y'$ corresponding to the x and y components of the linearly polarized light after the prism .

$$
\begin{aligned}
I_x &= \frac{I_0}{2}(1 - sin\Delta\phi) \approx \frac{I_0}{2}(1 - \Delta\phi) \\
I_y &= \frac{I_0}{2}(1 - sin\Delta\phi) \approx \frac{I_0}{2}(1 + \Delta\phi)
\end{aligned}
\tag{9.6}
$$

Equation 9.6 describes the linear relation between the rotation angle and the current signal, combining with the linear electric field dependence of Pockels effect, we can establish a linear relation of the signal and the THz amplitude.

9.5   Data analysis

To quantitatively describe the optical rotation and ellipcity of the transmitted THz light in the frequency domain, we can measure the *x* and *y* components

of the light, and then calculate the righ-hand and left-hand circularly polarized light:
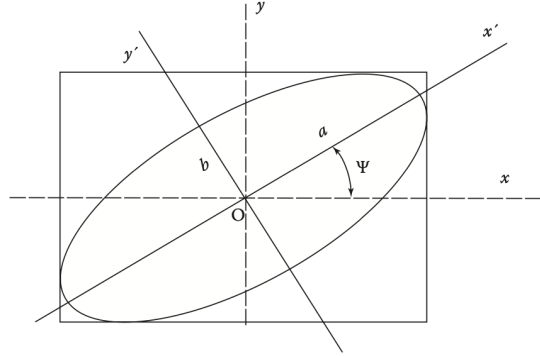
FIGURE 9.8: The optical ellipse.

$$\tilde{E}_{CRA}(\omega) = \frac{\tilde{E}_x + i\tilde{E}_y}{\sqrt{2}}$$
$$\tilde{E}_{CRI}(\omega) = \frac{\tilde{E}_x - i\tilde{E}_y}{\sqrt{2}} \tag{9.7}$$

Then by plugging into the equation 9.8 and equation 9.9, one can get to rotation angle θ and ellipticity η, which are demonstrated in figure 9.8[31].

$$\Psi(\omega) = \frac{arg[\tilde{E}_{CRA}(\omega)] - arg[\tilde{E}_{CRI}(\omega)]}{2} \tag{9.8}$$

$$\eta(\omega) = \frac{|\tilde{E}_{CRA}(\omega)| - |\tilde{E}_{CRI}(\omega)|}{|\tilde{E}_{CRA}(\omega)| + |\tilde{E}_{CRI}(\omega)|} \tag{9.9}$$

By conducting the sample-reference measurement with normal incidence, one can easily extract the complex refractive index of a materials by knowing the refractive index of the reference[32]. Here in our measurement, we use free-space as reference by assuming the refractive index of air $n_{air} = 1$. The experiment configuration is shown in figure 9.9. Considering different components of the sample signal, one can write the emitted electric field as:

$$E_{samp}(\omega) = T_{12}(\omega) \cdot P_2(\omega) \cdot T_{21}(\omega) \cdot FP(\omega) \cdot E(\omega) \tag{9.10}$$
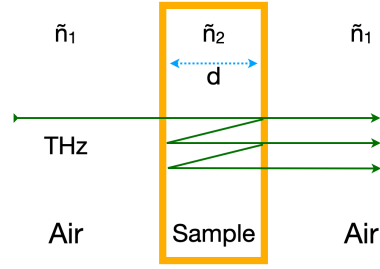
FIGURE 9.9

where the Fabry Pérot term FP(ω) is:

$$FP(\omega) = \sum_{k=0}^{\infty} [R_{21}(\omega) \cdot P_2^2(\omega) \cdot R_{21}(\omega)]^k \tag{9.11}$$

The Fresnel equations of normal incidence are:

$$R_{12}(\omega) = \frac{\tilde{n}_1 - \tilde{n}_2}{\tilde{n}_1 + \tilde{n}_2} \tag{9.12}$$

$$R_{21}(\omega) = \frac{\tilde{n}_2 - \tilde{n}_1}{\tilde{n}_1 + \tilde{n}_2} \tag{9.13}$$

$$T_{12}(\omega) = \frac{2\tilde{n}_1}{\tilde{n}_1 + \tilde{n}_2} \tag{9.14}$$

$$T_{21}(\omega) = \frac{2\tilde{n}_2}{\tilde{n}_1 + \tilde{n}_2} \tag{9.15}$$

The amplitude decay introduced by the sample is:

$$P_2(\omega) = e^{i\frac{\tilde{n}_2 \omega d}{c}} \tag{9.16}$$

where $\tilde{n}_a = n_a + i\kappa_a, a = 1, 2$, d is the thickness of the sample. The transmitted amplitude through free-space is:

$$E_{ref}(\omega) = P_1(\omega)E(\omega) \tag{9.17}$$

By comparing the difference between the sample and reference:

$$\frac{E_{samp}(\omega)}{E_{ref}(\omega)} = \frac{4\tilde{n}_1\tilde{n}_2}{(\tilde{n}_1 + \tilde{n}_2)^2} exp[i\frac{(\tilde{n}_2 - \tilde{n}_1)\omega d}{c}] \tag{9.18}$$

Assuming $n_a >> \kappa_a$ and take $\tilde{n}_1 = 1$ for air, one can get

$$n_2(\omega) = 1 + \frac{c}{\omega d} phase[\frac{E_{samp}(\omega)}{E_{ref}(\omega)}]$$

(9.19)

$$\alpha_2(\omega) = -\frac{2}{d} ln \frac{|\frac{E_{samp}(\omega)}{E_{ref}(\omega)}|}{|T_{12}T_{21}|}$$

(9.20)

Chapter 10

KTaO$_3$

10.1 Introduction

Ultrafast optical control of structure in perovskites and their relatives has been
of great interest in studying nonlinear phononics and laser-induced phase tran-
sitions, including the transitions to metastable hidden phases[33, 34, 34–36]. In
particular, the nonlinear coupling between the infrared-active soft mode and
first-order Raman-active modes provides a new path for lattice modulation[37–
39]. The zone-center IR-active soft mode plays a key role in the phonon-phonon
interaction picture in the perovskites. As the temperature decreases, the soft
mode gradually softens, the material either undergoes a ferroelectric phase
transition at Curie temperature, for example BaTiO$_3$[40, 41], or arrives at a so
called *quantum paraelectric state* without any long range polar orders down to
0 K, such as SrTiO$_3$ (STO) and KTaO$_3$ (KTO)[42–44]. The quantum paralectric
state results from the competitions among antiferrodistortive (AFD) structural
phase transition, ferroelectric ordering and quantum fluctuation below certain
threshold temperatures[45].

KTaO$_3$ is one of the perovskite family compounds which has been intensively
studied since the middle of last century [42, 43, 46–49]. KTO has a simple
cubic structure with space group *Pm$\bar{3}$m* (*No.*221) at room temperature and
holds the cubic structure down to at least 10 K which is out of our research
scope[42, 49]. KTO single crystal exhibits many novel physical properties such
as two-dimensional electron gas[50], superconductivity under electrostatic car-
rier doping[51], metal-insulator transitions[52]. KTO is also well known as a

quantum paraelectric material, the temperature dependence measurements show that the dielectric constant of KTO increases continuously as the temperature cools down to 8 K and levels off to 0 K without undergoing ferroelectric phase transition[53]. More interestingly, even though the long range ferroelectric order is banned at low temperature, but the local polar phase can still exist with $R_0/a \approx 4$ in both doped and nominally pure KTO[43, 44]. So at the low temperature regime, the phase diagram of KTO crystal is almost temperature independent, but very sensitive to the external stimuli, such as electromagnetic irradiation or strain. These properties make KTO an ideal material for studying nonlinear phononics and usltrafast optical control. The TO_1 soft mode in KTO can be described very well by the mean-field Barrentt formula[47, 54, 55]. By fitting the experimental data with Barrentt formula, Chen *et al.* found that the Curie temperature of KTO is 1.6 K, the temperature at which the instability begins is 32 K, and the dielectric constant depends significantly on the external dc electric field which agrees well with our measurements under THz field in the present work[54].

10.2 Methods

Here we report optical time-resolved studies of KTO where intense single-cycle THz pulses are used as the excitation. We use optical rectification in a $LiNbO_3$ prism and tilted-wavefront phase matching to generate the THz pulses from femtosecond pulses with 800 nm center wavelength. A small portion of the femtosecond pulse energy is split off before THz generation and is used as an optical probe pulse. We detect two quantities using the optical probe: one is the THz field induced second-harmonic generation (TFISH) and the other is the THz-induced polarization rotation (THz Kerr effect, or TKE). Both the TFISH and TKE are measured with the probe beam transmitted through the sample. For the TFISH experiment, the polarization directions of the THz beam and the optical beam are both chosen to be vertically polarized in the lab frame, while in the TKE experiment, the optical beam is 45° polarized from the vertically polarized THz beam. The TFISH intensity is measured using a GaP photodiode and a blue filter after the KTO sample, which eliminates the fundamental 800

nm wavelength from the detected light. The KTO sample used here is a commercial product from MSE Supplies cut in the (100) direction with double-side polished surfaces.

10.3 Result and discussion

KTO crystal possesses inversion symmetry, so that no second-harmonic generation can occur in the equilibrium state. The presence of the strong THz electric field breaks the inversion symmetry and causes a bulk polarization of the crystal and leading to the detection of the TFISH intensity. Therefore, TFISH light serves as an optical probe of polarization. The TFISH intensity rises with the arrival of the THz electric field and decays within a few picoseconds after the THz pulse. Only positive values of the TFISH intensity are recorded because it is measured as a difference in the intensity of the TFISH light with and without the THz field, and the latter intensity being zero. This is in contrast to TFISH measurements in non-centrosymmetric media where both positive and negative second-harmonic intensity can be observed.

FIGURE 10.1: (Color online) THz field induced second-harmonic generation spectra. (a) Time domain spectroscopy under various temperatures. (b) The frequency domain spectroscopy corresponding to the measurements in (a), the first derivatives of the interpolated time domain spectroscopy were calculated before the Fourier transformation to reduce the relative amplitude of the non-oscillatory signal. (c) Frequency domain spectroscopy under various THz electric fields at 15 K. Inset: The peak values of TFISH time domain spectroscopy vs. amplitudes of THz electric field, red dots are the experiment data and the blue solid line is the quadratic fitting curve.

Figure 10.1(a) shows the temperature dependence of the time domain TFISH signal. The peak strength of TFISH gradually diminishes with increasing temperature. In addition to the rise and decay of the intensity, we also find oscillations in the signal. The first three peaks in Fig. 10.1(a) are mainly driven directly by the THz pulse packet, while the remaining oscillations come from the relaxation of the stimulated phonon mode. Because the TFISH signal is measured using co-propagating THz pump and optical probe beams, it is necessary to consider their dephasing due to their different group velocities inside the medium. However, the penetration depth of the THz light in KTO at low temperature is less than 1 μm [47, 53], which means that the measured second-harmonic response originates from a thin 1-μm-scale layer near the front surface of the specimen and any dephasing effects on the measurement can be neglected.

Figure 10.1(b) shows the corresponding frequency domain spectra of the TFISH measurement, where the Fourier transform was performed on the first derivative of the time-domain signals in Fig. 10.1(a). The dependence of the frequency-domain spectra on the strength of the incident THz field at 15 K temperature is shown in Fig. 10.1(c). The THz field dependent TFISH is usually described as a $\chi_3(\omega_{THz}, \omega, \omega)$ process in nonlinear optics, the intensity of the signal is proportional to the square of the product $\chi^{(3)}(\omega_{THz}, \omega, \omega)E^{THz}(E^\omega)^2$, where E^{THz} denotes the THz electric field and E^ω denotes the electric field of the optical probe pulse. By fitting the THz field dependent TFISH signal with a quadratic function as shown in the inset of figure 10.1(c), the consistent fitting result further demonstrates that the TFISH signal comes from the third order $\chi_3(\omega_{THz}, \omega, \omega)$ process.

Figure 10.1(b) shows that the TFISH resonance peaks at 15 K is around 1.9 THz, which is roughly the double of the TO_1 soft mode frequency from the earlier works[42, 48, 53]. The frequency doubling can be understood by considering the soft mode motion of the Ta^{5+} cation relative to the O^{2-} anion octahedron in the KTO unit cell. The external THz field E^{THz} introduces a minute displacement of Ta^{5+} along z axis, which breaks the inversion symmetry of the crystal, but the total displacement of the Ta^{5+} cation is still dominated by the amplitude of the soft mode oscillation. Since second-harmonic generation only depends on the displacement of the Ta^{5+} cation from the equilibrium position, rather

than the directions, so the frequency of the TFISH signal doubles. The time resolution of our setup is 0.05 ps, while the TFISH period is about 0.5 ps which is one order larger than the resolution, so ideally we should have the capability to capture more sophisticated oscillation pictures than we actually have at hand. But unfortunately we can only observe a few peaks of oscillations at relatively high amplitude values in the TFISH signal, this deviation may come from two alternatively plausible reasons which need further exploration. (a) Different areas of the laser spots (both THz and optical) incident on the sample are not absolutely in phase, so the low intensity signals smear out at the GaP diode detector. (b) The skewing of the anharmonic mode function renders the probability of the Ta^{5+} cation in the intermediate region much lower than other places in the unit cell.

The complementary TKE measurement is conducted right after the TFISH experiment. TKE is a third order nonlinear optical effect describing the THz intensity dependence of the refraction index[9]:

$$n(I^{THz}) = n_0 + \frac{\chi^{(3)}(\omega_{THz}, \omega_{THz}, \omega)}{2n_0}(E^{THz})^2 = n_0 + n_2 I^{THz} \quad (10.1)$$

where n_0 is the linear part of the refraction index, $\chi^{(3)}(\omega_{THz}, \omega_{THz}, \omega)$ is another third order nonlinear susceptibility and $n_2 = \frac{\chi^{(3)}(\omega_{THz}, \omega_{THz}, \omega)}{n_0^2 c \epsilon_0}$. The refraction index of the specimen in our case changes along the E^{THz} field direction and is proportional to $(E^{THz})^2$ according to equation (10.1). More details of TKE measurement with significant fundamental THz pulse overlap in noncentrosymmetric materials are described in our earlier work[56].

Figure 10.2(a) shows the temperature dependence of the time domain TKE spectra. The THz field changes the refraction index of the specimen along electric field vector introduces optical birefringence. We observed similar oscillatory behavior in the TKE measurement in Fig. 10.2(a) as in TFISH, Fig. 10.1(a). But the non-oscillatory component relaxes much slower than that in TFISH measurement, specifically $\tau_{TKE} > 100$ ps at 8 K while $\tau_{TFISH} < 10$ ps at 11 K. The dashed line in figure 10.2(b) shows clear tendency of the mode softening as the temperature decreases, so we assign this mode to A_{2u} mode. This observation is in contrast with Xian's work on $SrTiO_3$ crystal which is both qualitatively and quantitatively similar with KTO. In their work, they assigned the 1.3 THz mode from the TKE measurement which has no obvious mode softening to the
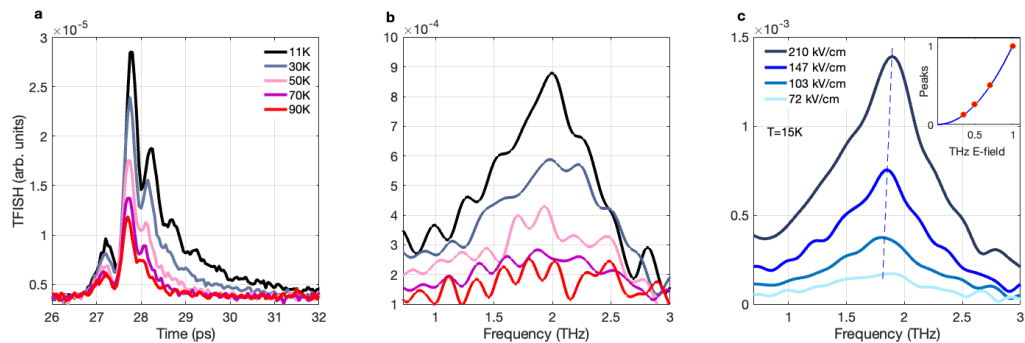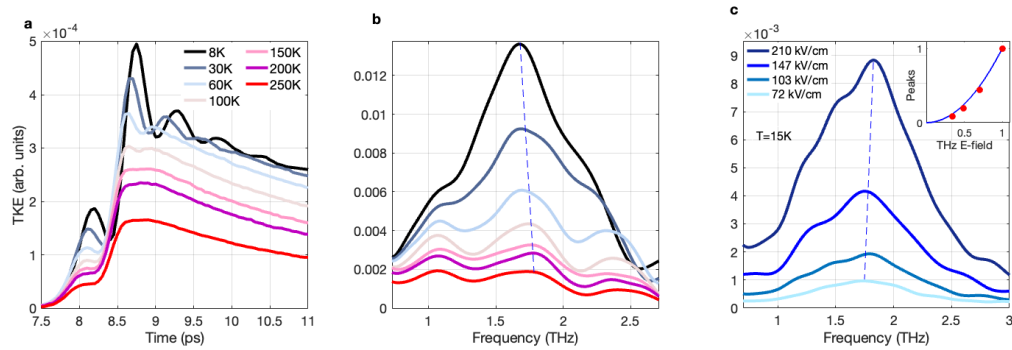
FIGURE 10.2: (Color online) THz field induced Kerr effect spectra. (a) Time domain TKE spectra under various temperatures. (b) The frequency domain spectroscopy corresponding to the measurements in (a), the blue dashed line is used to show the shift of peaks. (c) Frequency domain spectroscopy under various THz electric field at 15 K. Inset: the peak values of TKE time domain spectroscopy vs. amplitudes of THz electric field, red dots are the experiment data and the blue solid line is the quadratic fitting curve.

A_{1g} Raman mode and the A_{1g} mode anharmonically coupled with the A_{2u} soft mode which agrees well with the theoretical prediction[33, 48]. Figure 10.2(c) shows the THz field dependence of the TKE signal with a blue dashed line showing the peak shift. The resonant frequency of the soft mode increases as we increase the external field, and we have the similar observation in the TFISH measurement in figure 10.1(c), this agrees well with the field dependent behavior of the soft mode in the earlier work[48] and it further strengthens our mode assignment argument. In the mean time, this field dependent behavior sketches the onset of the field induced nonlinear effect in the soft mode. The inset of figure 10.2(c) exhibits a quadratic behavior of the time domain TKE peak vs. THz field which is described by function (10.1) for TKE effect.

Figure 10.2(b) shows that the soft mode frequency is also doubled the same as the TFISH measurements. But the mechanism underlying is quite different. The TKE measurement detects the change of refraction index of the crystal, or in other words, the change of polarizability from the stand point of spectroscopist. We can express the polarizability as a series of mormal coordinates **Q** of the crystal[57]:

$$\alpha = \alpha_0 + \sum_k (\frac{\partial \alpha}{\partial Q_k})Q_k + \frac{1}{2}\sum_{k,k'}(\frac{\partial^2 \alpha}{\partial Q_k \partial Q_{k'}})Q_k Q_{k'} + ... \quad (10.2)$$

With the lattice wave equation:

$$Q_k = A_k e^{\pm i(\mathbf{k}_k \cdot \mathbf{r} - \omega_k t)} \quad (10.3)$$

The linear term of Q_k in equation (10.2) is responsible for the first-order Raman scattering, while the quadratic term accounts for the second-order effect. Since the KTO crystal has cubic structure with inversion symmetry, all long-wavelength phonons at Γ point in k space have odd parity. As a result, the first-order Raman scattering in equation(10.2) is forbidden by the selection rule. But the second-order Raman scattering is alowed, and if we plug the lattice wave function (10.3) into the second term of the polarizability function (10.2), we will get the expression for the two-phonon response of the Raman scattering which describes the observed frequency-doubling behavior in our TKE measurement exactly[49, 58].
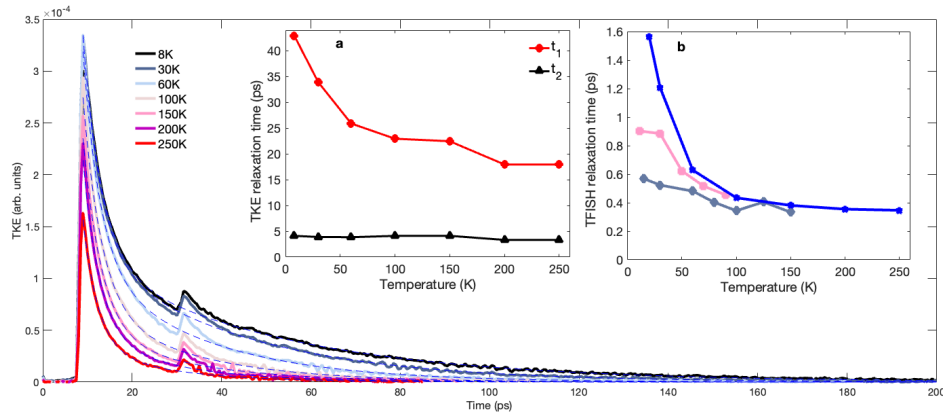
FIGURE 10.3: (Color online) Long time range THz field induced Kerr effect spectra. The main figure shows long time domain TKE spectra vs. temperature. The dashed blue lines are the fitting curves with the biexponential function: $f = Ae^{\frac{-(t-t_{01})}{t_1}} + Be^{\frac{-(t-t_{02})}{t_2}}$. The inset figure(a) is the extracted relaxation time from the main figure curve-fittings. The extracted relaxation times from different TFISH measurements using the exponential function: $f = Ae^{\frac{-(t-t_{01})}{t_1}}$ are plotted in the inset figure(b).

Figure 10.3 shows the long time range TKE measurements and the fitting relaxation time vs. temperature. The main figure is the soft mode relaxation versus different temperatures, the small kinks at 31 ps are due to the reflection of silicon wafer in the upper THz stream. We used a biexponential function to fit the relaxation behavior, and the two different relaxation times are plotted in figure 10.3(a). The shorter relaxation time t_{TKE2} in black triangles behaves more like a constant with the value about 4 ps, while the relaxation time t_{TKE1} in red closed circle is much larger than t_{TKE2} and increases from 18 ps to 43 ps as the temperature decreases. As a comparison, we also plotted the relaxation time t_{TFISH} from TFISH measurement in figure 10.3(b) from three different measurements. The relaxation time from TFISH increases even faster than t_{TKE1} from 0.35 ps to 1.57 ps but with much smaller values.

By far, the most striking thing arises from the two complementary measurements is the huge difference between the non-oscillatory relaxation time t_{TKE1} and τ_{TFISH}. The dramatic difference indicates two basically different interaction pictures underlying the TKE and TFISH measurements but bridged by the same ferroelectric soft mode. Here we provide a qualitative explanation from the perspective of different interaction ranges of electric dipoles and quadrupoles, further theoretical calculation is needed in the future work. The electric dipole moment of the soft mode in KTO can be described by $\mathbf{p}_{dip,z} = q\mathbf{Q}_z$, where q is the effective charge and Q_z is the displacement of normal mode along z direction. The attenuation rate of a dipole moment potential is $\sim \frac{1}{r^2}$, where r is the distance between different electric dipole moments. So the interactions of the dipole moment with the environment decay in a way of $\sim \frac{1}{r^2}$. By the same token, for the Raman active mode in TKE measurement, considering the expression in equation (10.2), we can generally describe it in a way analogous to electric quadrupole with expression $p_{quad,z} \sim q\mathbf{Q}_z^2$ and the attenuation rate of the quadrupole potential is $\sim \frac{1}{r^3}$. From this angle of view, since the potential of electric quadrupole decays much fast in space than its counterpart, namely electric dipole, the ineractions of the quadrupole with its environment decay much faster than electric dipole, so we could expect to observe a much longer relaxation time in the TKE signal than the TFISH.

10.4   Summary

In summary, from the complementary TFISH and TKE measurements on quantum paraelelctric material KTO, we observed the ferroelectric mode softening with decreasing temperature. The mode assignment is supported by the increasing frequency of the soft mode under external electric field. We explained the totally different mechanisms of the soft mode frequency doubling in these two measurements. Most strikingly, we observed dramatically different relaxation times from TFISH and TKE measurements, and qualatitively explained it using electric dipole and quadrupole models. Generally speaking, our results demonstrate an extremely clear microscopic picture of the ferroelectric soft mode oscillation under THz field induced symmetry breaking in KTO and it paves the way for the further study of ultrafast optical control in perovskite family. In addition, the dramatically different IR and Raman responses from the same THz pulse excitation provide a very unique angle for the study of nonlinear phononics, and reveals a deeper insight in the path of the resonant mode energy dissipation between different mechanisms bridged by the same mode.

Chapter 11

BaCoSiO$_4$

11.1 Introduction

Optical active materials have the power to rotate the plane of linearly polarized light beam. The first optical active material - quartz crystal, was found by a French scientist Arago in 1811. Optical active materials are said to exhibit *natural optical activity(OA)* in the absence of external influences such as magnetic field **B**[59]. Materials with chiral crystal structures are closely related to the optical activity phenomenon. Chiral materials are those that the images of their crystal structures cannot coincide with themselves by any sequence of rotation and translation operations. Chiral materials with the point group $1, 2, 222, 4, 422, 3, 32, 6, 622, 432$ and 23 and the non-chiral materials with the point group $m, mm2, \bar{4}$ and $\bar{4}2m$ are all predicted to exhibit OA [60]. The OA phenomenon exhibited in chiral materials are generally ascribe to the distributions of electrons in the crystals[61].

Natural circular dichroism(NCD) and *rotatory dispersion spectroscopy* are powerful tools to study electric and vibrational excitations of states for chiral materials in sterochemistry and condensed matter physics[62]. By studying NCD and rotatory dispersion of the transmitted linearly polarized light, we can get the information of the refraction index n and absorption coefficient α of the medium for the right and left handed circular polarized light respectively. Here in the present section, we conducted the terahertz time-domain spectroscopy (THz-TDS) measurement to investigate the NCD and rotatory dispersion in $BaCoSiO_4(BCSO)$.

Due to their complex polymorphism, the derivatives of the tridymite (SiO_2) are good model systems to study the changes of tetrahedral frameworks induced by atom replacing[63]. The structures and UV range optical properties of the compound $Ba(Co_{1-x}Zn_x)O_4$ were closely investigated as candidates of new photo-catalytic materials because of its relatively small band gap[64]. Strong photo-induced dielectric response was observed in one of the derivatives: BCSO[65].

BCSO is a Mott insulator with a tetrahedral porous network. Three crystallographically independent Ba^{2+} kations with different coordination environments are stuffed into the voids of the structure as shown in figure11.1(a). The Co^{2+} kations surrounded by oxygen anions form octahedral sublattices and occupy high-spin state with spin 3/2. BCSO belongs to hexagonal space group of $P6_3(NO.173, Z = 6)$ corresponding to point group C_6. The gyration tensor of point group C_6 has no zero element which indicates that BCSO has a chiral structure that breaks the space inversion symmetry[60]. Fisrt-principle calculations predict a sharp density of states at the bottom of the conduction band around $2eV$ suggesting fairly localized excited electrons [63, 64]. The temperature dependent magnetization measurement of BCSO shows a antiferromagnetic transition at 3.2K, from 3.2K up to room temperature, BCSO is in paramagnetic state, figure 11.2. BCSO has intricate magnetic structures as shown in figure 11.1 (b) and (c). To appreciate the toroidal nature of the antiferromagnetic groud state below 3.2K, three sublattices with red, cyan, and blue colors are marked, each of which is a network of trimers forms nonzero toroidal moment. The three sublattices form a antiferrotoroidal ground state under zero magnetic field, but can flipped into ferrotoroidal state by applying an external magnetic field $B = 1.2T$ at 1.5K[66].

11.2 Methods

Spectroscopy: we used a femtosecond mode-locked Ti: sapphire laser source (center wavelength: 800nm, pulse width: $35fs$, repetition rate: $1000Hz$). The homemade zero-field THz time domain spectroscopy (THz-TDS) was used to detect the absorption and rotation of BCSO crystal under Faraday geometry. The THz pulse was generated by optical rectification in Lithium niobate ($LiNbO_3$).
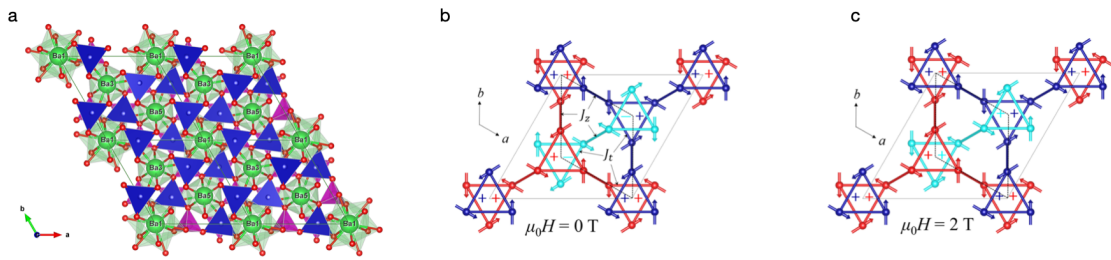
FIGURE 11.1: (a) $BaCoSiO_4$ crystal structure in c direction. Ba1, Ba3, Ba5 atoms all located on threefold axes but have different coordinate environments, we can tell this from the orientations of the different CoO_4 sublattices at the equivalent positions relative to Ba^{2+} anions. (b) Magnetic ferritoroidal ground state at $B = 0T$. (c) The ferritoroidal ground state is changed into ferrotoroidal state under $B = 2T$[66].
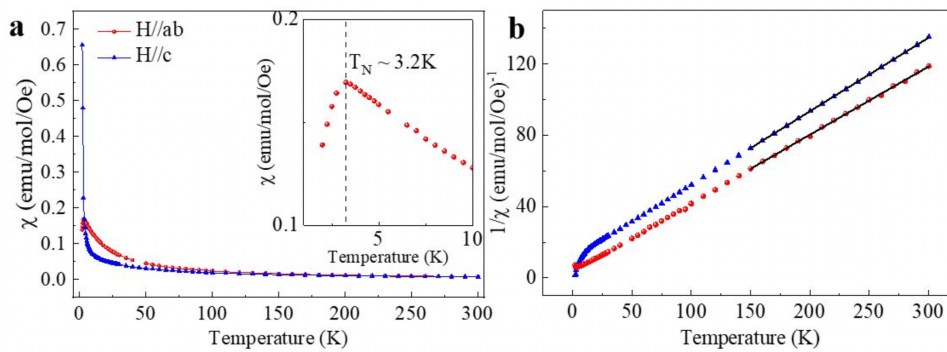
FIGURE 11.2: $BaCoSiO_4$ magnetization measurement. (a) The temperature dependence of the magnetic susceptibility along c axis and in ab plane with magnetic field ($B = 0.1T$). (b) Inverse magnetic susceptibility curves and the corresponding fits using the Curie-Weiss law[66].

The actual electric field of the THz pulses with accurate amplitude and phase was measured by free-space electro-optic sampling using a $ZnTe$ crystal. The THz Spectroscopy in high magnetic fields ($-17T$ to $17T$) were performed using photo-conductive antennas as THz emission and detection. The polarization of the incident THz beam is controlled by a wire-grid polarizer. The transmitted x, y component of the THz light was picked out by a wire-grid analyser. More detailed setups are introduced in our previous work[67].

Magnet: for the field-dependent measure of BCSO, the sample was mounted in the chamber of J4839 17T cryogen-free magnet, the temperature range from 4K to 300K, the magnetic field can change continuously from $-17T$ to $17T$.

Sample: we used two BCSO samples from different batches in this experiment.

Sample-#1 was cut perpendicular to *c* axis of the crystal, with the normal direction of the cutting plane off the *c* axis less than 3°. Sample-#2 was cut off *c* axis 27.5°. Both samples were grounded into thin plate with polished surface.

DFT calculation: in our theoretical calculation, we used the frozen phonon method[68] for the force constant and dynamic matrix calculation[69]. Then solve the dynamic matrix we can have the phonon band structure. On each point of the band structure, the eigen mode can be generated and the polarization change in the eigen mode can be calculated using Berry phase with Born effective charge correction.

11.3   Results and discussion

We conducted THz ellipsometry measurement along *c* axis of the BCSO crystal sample-#2 without magnetic field firstly, the rotation and ellipticity measurements show a lattice vibrational mode lies between $0.6 - 0.7THz$, figure 11.3. The amplitude of the phonon mode smear out gradually into the thermal fluctuation background as the temperature raises above $60K$, figure 11.3(a). By using Local-density approximations+U method, we calculated the phonon band as shown in figure 11.6(a), which shows the lowest phonon mode at Γ poit is about $0.923THz$, the energy shift between the experimental result and the theoretical calculation may stem from the defects or doping in the BCSO crystal, and we do observe a slight shift of the resonant peaks between BCSO sample-#1 and #2 from different batches by comparing figure 11.3(a) and figure 11.4(a)(b).

Since the crystal structure of BCSO is chiral, from the knowledge of SOS we know that by applying an external magnetic field along the chiral axis *c*, one would expect to observe optical non-reciprocity with counterpropagating THz beam in this configuration. We studied the THz rotation and ellipticity of BCSO under $\pm \boldsymbol{B}$ field, the non-reciprocal effect becomes more and more significant as the magnetic field increases from 0 to $17T$ as shown in figure 11.3(b)(c).

Chiral materials are naturally optical active, despite the other possible mechanisms, the rotation power of optical active materials along the chiral axis is isotropic, this means one would expect to observe polarization-independent rotation power from BCSO along *c* axis. We conducted incident polarization-dependent measurements on both BCSO sample-#1 and #2 in figure 11.4. From
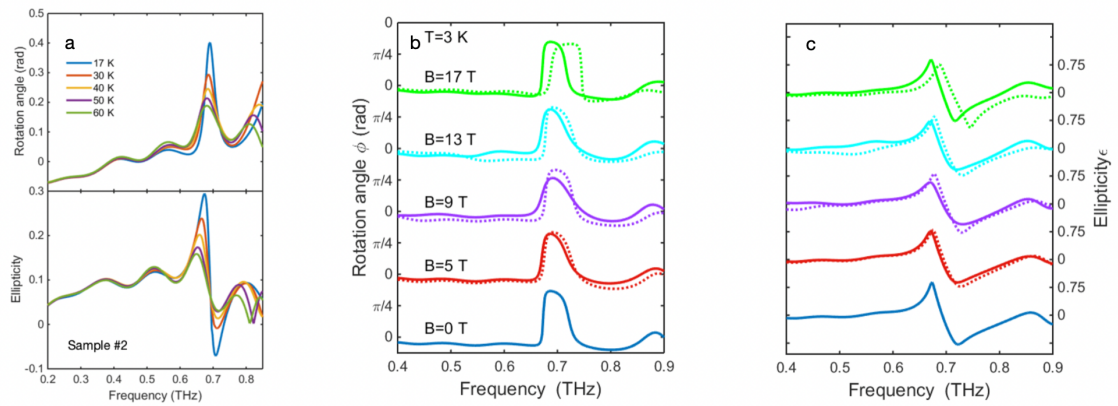
FIGURE 11.3: BCSO phonon mode and THz non-reciprocity(a) BCSO optical rotation and ellipticity as a function of temperature. (b)(c) THz non-reciprocity of BCSO can be observed from both field-dependent optical rotation and ellipticity.

figure 11.4(a)(b), we find that the ellipticity and rotation angles are dependent on the polarization directions of the linearly polarized incident light, the rotation angles range from $-6°$ to $-15°$ as we sweep the incident angle from $0°$ to $60°$. Then we studied the ellipticity and absorption on sample-#2 with the incident polarization $90°$ apart from each other. The ellipticity flips sign after $90°$ rotation indicating a two-fold rotational symmetry in the crystal. This observation is also supported by the absorption measurement, at $80°$ of incident polarization, the resonant absorption is suppressed, but shows up after $90°$ rotation as shown in figure 11.4(d).

To better understand the optical non-reciprocity and magnetic structure of BCSO, we studied the angle-dependent transmission and ellipticity as a function of external magnetic field on sample-#2, figure 11.5. For the incident angle $20°$ and $70°$, figure 11.5 shows the relative transmission and the ellipticity of the sample-#2 under $\pm B$. The relative transmission and ellipticity with opposite directions are different under various magnetic field, which indicating optical non-reciprocity as we have discussed earlier in figure 11.3. In addition, we can observe significant magnetic spin resonances with different external magnetic fields which are marked with double-side arrows in different colors, the magnetic resonance changes the absorption and ellipticity of the transmitted THz light.

As we have discussed earlier, the rotational power of optical active materials should be the same along the chiral axis, but we observed angle-dependent
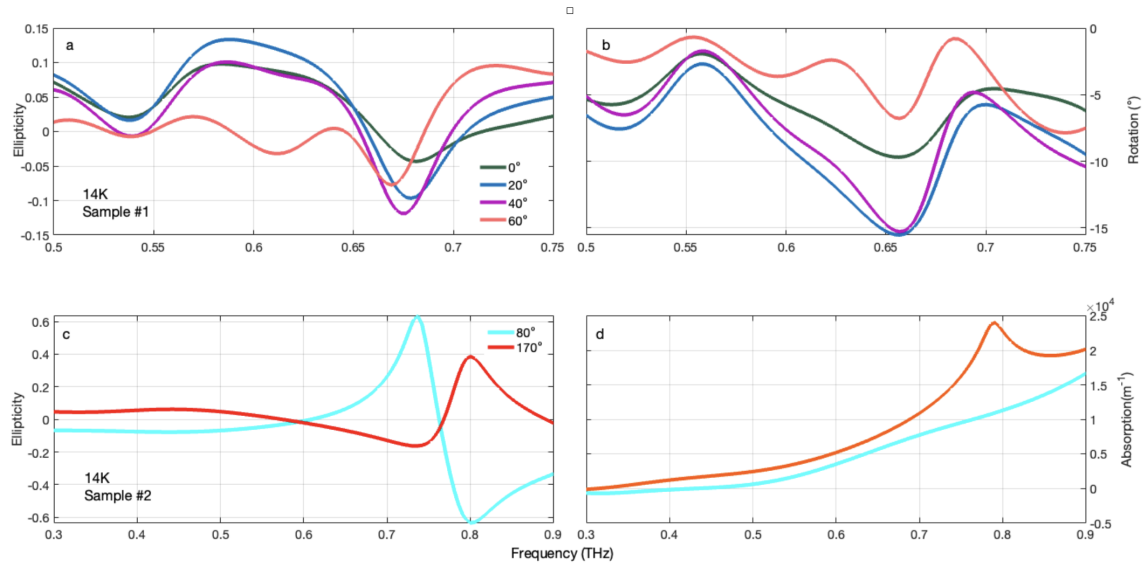
FIGURE 11.4: Anisotropy of BCSO in the *ab* plane. (a)(b) Rotation and ellipticity as a function of incident linearly polarized light at 14*K* for sample-#1 of BCSO. (c)(d) Two-fold rotational symmetry of BCSO sample-#2 at 14*K*. The sign of the ellipcity flips in (c) and the absorption resonance disappears by the 90° rotation of the incident polarization of the THz light.

rotational power in both samples. Since BCSO is an uniaxial material, it is reasonable to have two-fold rotational symmetry in the plane of sample-#2 with an angle 27.5° off the *c* axis of the crystal, but not for sample-#1 with an angle $< 3°$. From the theoretical calculation, we find that the lowest energy phonon mode forms a inbuilt polarization along *c* axis as shown in figure 11.6(b). From the discussion of Pockels effect in the earlier chapters, we learned that second-order nonlinear effect of crystal with the electric field launching along *c* axis will introduce birefringence in the *ab* plane of the crystal just as what happened in the typical nonlinear crystal KH_2PO_4.

11.4 Summary

In summary, we investigated the THz non-reciprocity of BCSO under the external magnetic field along *c* axis of the crystal, which is predicted by SOS methods for chiral materials, the experimental results demonstrate that that non-reciprocal effect is tunable by adjusting the amplitude of the magnetic field. We observed THz anisotropy in the *ab* plane of BCSO from the polarimetry measurement, this phenomenon is probably due to the birefringence in the *ab* plane
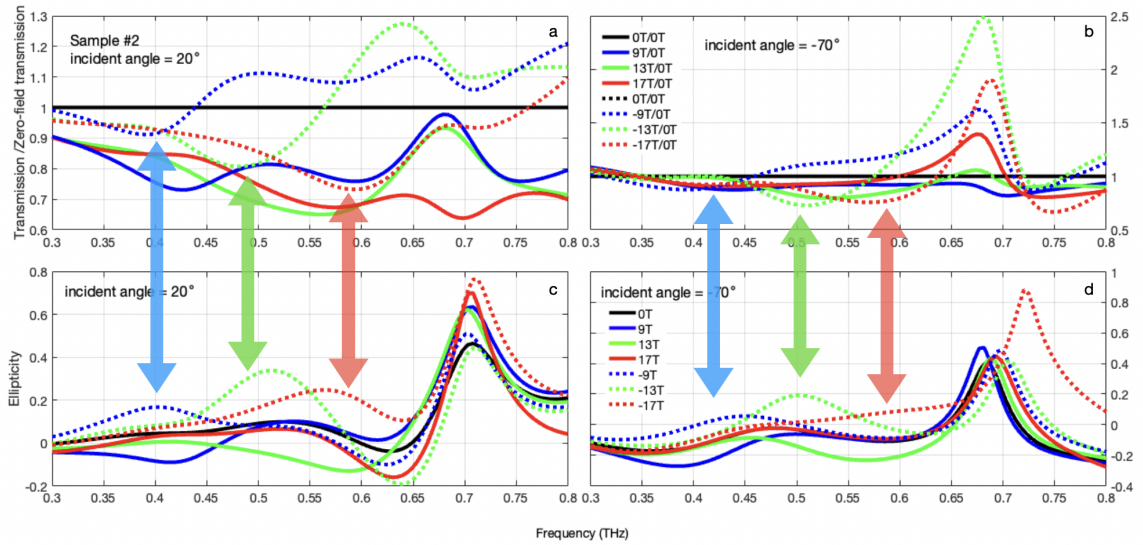
FIGURE 11.5: Transimission and ellipcitiy of BCSO as a function of external magnetic field with the incident angle $90°$ apart from each other. For $\pm B$, the transmission exhibit non-reciprocal effect for both measurements.Except optical non-reciprocal effect, we can also observe magnetic spin resonance with the resonance frequency proportional to the magnetic field, the corresponding resonant peaks are marked by arrows in different colors.
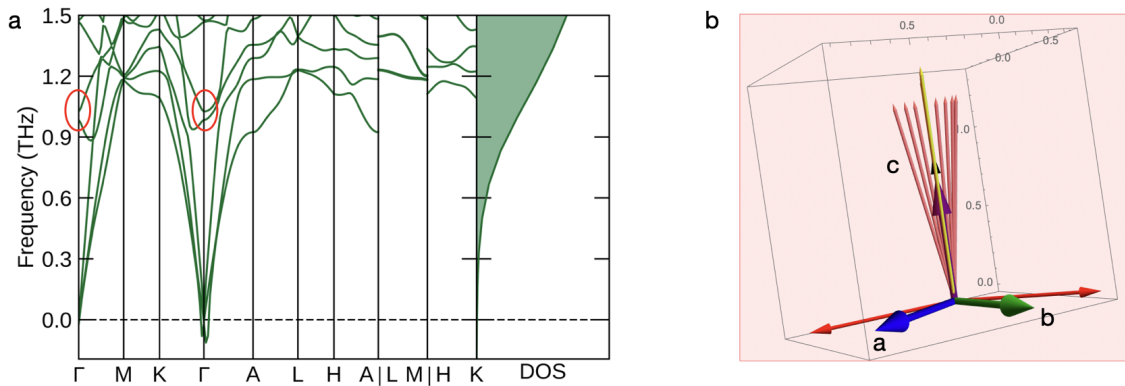
FIGURE 11.6: DFT calculation of BCSO. (a) Phonon band and density of state. The lowest two optical modes at $0.923 THz$ and $0.988 THz$ on Γ point are marked with red circles. (b) Polarizations of the two lowest optical mode, the yellow arrows are for $0.923 THz$ mode and the salmon arrows are for $0.988 THz$ mode.

induced by the spontaneous polarization in the material which is supported by the DFT calculation.

Chapter 12

FeMn$_2$O$_4$

12.1 Introduction

Spinel family crystals have historically been one of the most highly revered gemstones due to its diversely beautiful colors. In modern industry, spinel crystals are widely used in battery and memory devices. Compounds from this family can also be used as spin filters in spintronics due to the asymmetry of the spin-polarized density of states around the Fermi energy, where one of the spin channels is a conductor while the other one behaves as an insulator[70, 71].
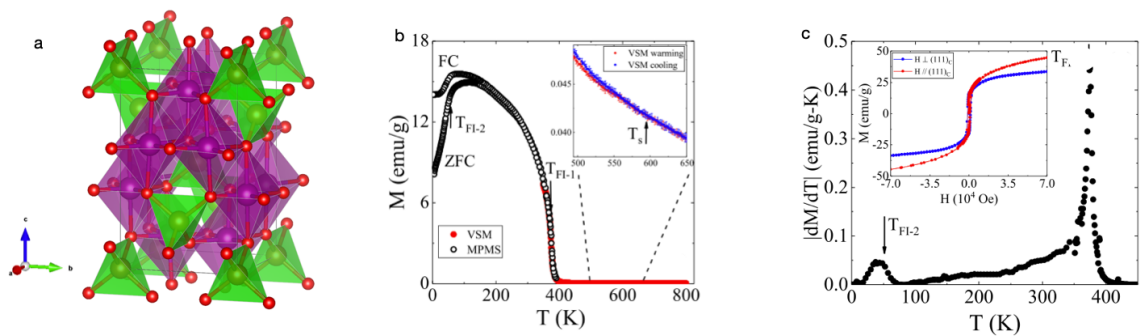
FIGURE 12.1: (a) FMO crystal structure[72].(b) Magnetization of FMO as a function of temperature[73]

The FeMn$_2$O$_4$ (FMO) that we studied in this article has an inverse spinel structure with half manganese atoms and all iron atoms in the octahedron sublattices

(*O* sublattice) and the remaining manganese atoms in the tetrahedron sublattices (*T* sublattice). FMO has a structure phase transition at $T_s \approx 595K$ from cubic structure at higher temperature to tetragonal structure (*I*41/*amd*, No. 141) at low temperature as seen in figure 12.1(a), due to a cooperative Jahn-Teller distortion of the MnO$_6$ octahedra. The superexchange interaction between *O* sublattices and *T* sublattices are much stronger than the interaction within the same sublattices, so typically, ions in different types of sublattices interact ferrimagnetically, while ions within the same kind of sublattices interact ferromagnetically. Since the number of *T* sublattices is less than the *O* sublattices, the ferrimagnetic state is developed. FMO has two ferrimagnetic phase trasitions at $T_{FI-1} \approx 373K$ and $T_{FI-2} \approx 50K$ respectively, figure 12.1(a)(b), the first phase transition is collinear while the second one is noncollinear. The magnetic easy axis of FMO is along [111] direction of the crystal structure[73].

12.2   Methods

Single-crystalline FMO was provided by our collaborators from LSU, it was grown by using a two-mirror optical floating zone furnace. For more details, readers can refer to the reference article from Roshan Nepal[73].

THz-TDS was performed using a home-built spectrometer based on a 1-kHz repetition rate regenerative Ti:Sapphire laser amplifier, equipped with He flow cryostat *J*4839 17*T* cryogen-free magnet that allows sample temperature control in the $4 - 300$ K range.

In order to study the magnetic spin waves with different polarization directions in FMO, we conducted THz time-domain spectroscopy under two distinct configurations, Faraday geometry and Voigt geometry, respectively, figure 12.2. For both of these two configurations, the THz light beam propagates along the [111] direction of the FMO crystal, the only difference lies on the direction of external B field. For the Faraday geometry, the THz light beam is parallel with the B field, and the polarization direction of the THz light is horizontal, while for the Voigt geometry, the THz light beam propagates perpendicularly to the external B field and the polarization direction of the THz light is also parallel with the B field.
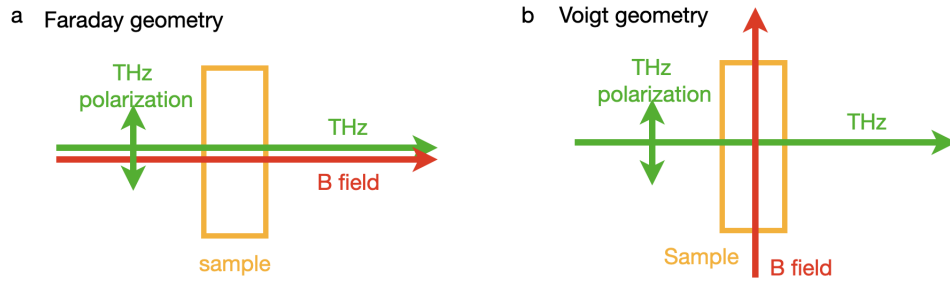
FIGURE 12.2: Different configurations for FMO measurement.(a) Faraday geometry.(b) Voigt geometry

12.3 Results and discussion

We first conducted THz transmission measurement for both Faraday and Voigt geometry with opposite B field directions at low temperatures. From the transmittance in figure 12.3(a) at $17T$, it is obvious to see that these two configurations behave drastically different. In Faraday geometry, THz non-reciprocity shows up with the opposite directions of B field. For $B = 17T$, two resonant peaks can be observed at $0.54THz$ and $0.34THz$, respectively, . While for $B = -17T$, one resonant peak shows up at $0.68THz$, but the other one at lower frequency at $0.38THz$ splits into two peaks. In the Voigt geometry, one broad resonant peak at $0.58THz$ is observed, and a smaller one shows up at $0.85THz$. The most interesting observation from Voigt geometry is that the transmittance for $B = \pm17T$ match very well, no non-reciprocal effect is observed as in the Faraday geometry.

We further studied the magnetic field-dependent THz transmittance at low temperatures for FMO, figure 12.3(b)(c). As the value of B field increase from $5T$ to $17T$, the spin resonance frequencies raise higher. But the optical non-reciprocity in Faraday geometry and the optical reciprocity in Voigt geometry are consistent despite the variation of B field.

By using an analyser after the FMO sample in the THz stream, we measured the x and y components of the transmitted THz light individually, combining these two measurements, we calculated the ellipticity of the transmitted light at $3K$ and $40K$ in Faraday geometry, figure 12.4. First of all, in all these ellipticity measurements, optical non-reciprocity sustained, the resonant peak positions in the frequency domain are systematically shifted for $\pm B$, and the
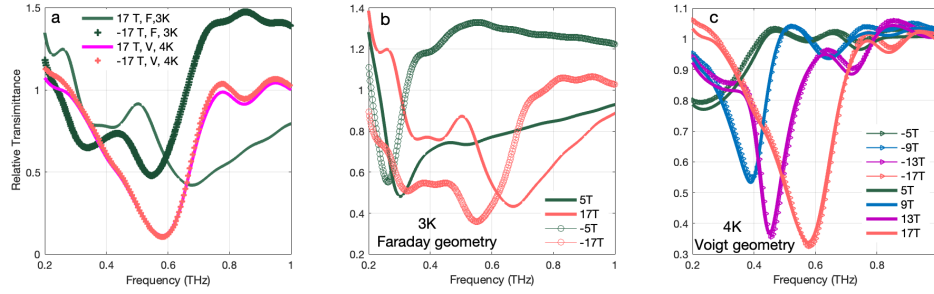
FIGURE 12.3: FMO transmittance under Faraday and Voigt geometry.(a) The transmittance of FMO at $\pm 17T$, in Faraday geometry, the transmittance exhibits THz non-reciprocity, while for Voigt geometry, it is reciprocal.(b) Non-reciprocity of Faraday geometry at $\pm 5T$ and $\pm 17T$.(c) Transmittance of FMO in Voigt geometry is reciprocal under various magnetic fields.
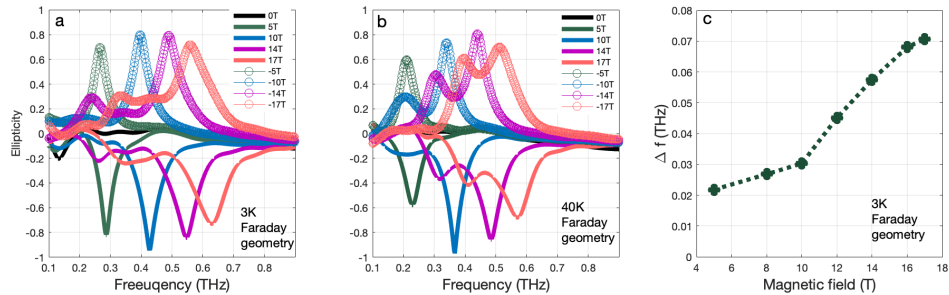
FIGURE 12.4: Ellipticity of FMO in Faraday geometry. (a) Ellipticity from $-17T$ to $17T$ at $3K$. (b) Ellipticity of FMO from $-17T$ to $17T$ at $40K$. (c) Main ellipticity peak shift between counterpropagating THz beam under various magnetic fields at $3K$.

field-dependent shifts of the main peaks at $3K$ is plotted in figure 12.4(c). Below $\boldsymbol{B} = 10T$, the spin resonant frequency increases linearly with the external magnetic field, which satisfies the magnetic resonant equation for ferromagnetic $\omega_0 = \gamma(B_z Hz)^{1/2}$, while for magnetic field $\boldsymbol{B}$ above $10T$, the field-dependent resonant frequencies deviate from the linear behavior under lower field conterintuitively, which indicates possibly field-induced magnetic phase transitions. Secondly, from figure 12.4(a) it is obvious to see that there are three resonant

peaks above $14T$, which can be presumably related to the three different sublattices in FMO crystal, further proof is needed to confirm this conjecture. As the temperature increases to $40K$, one of the resonant peak disappears and the energy gap of the remaining two resonant peaks shrink, based on this tendency, it is reasonable to infer that the remaining two may merge into one resonant peak at higher temperature eventually, and this is supported with the reported collinear ferrimagnetic phase transition at $50K$[73].
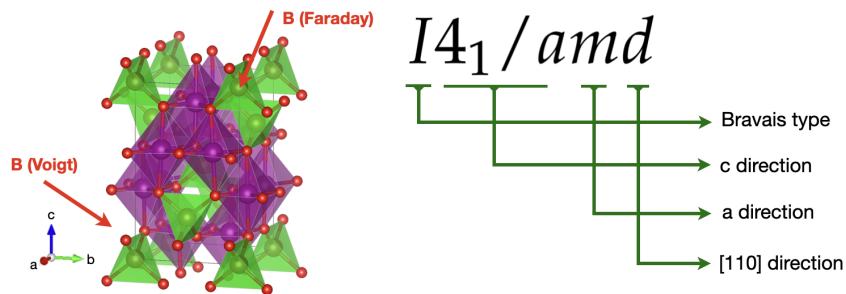
FIGURE 12.5: Symmetry analysis of FMO crystal structure with external $\boldsymbol{B}$ field.

Now let's get back to the THz non-reciprocity in FMO and try to use the SOS method to understand the symmetry difference between Faraday geometry and Voigt geometry in this material. Figure 12.5 demonstrates the relative positions of the magnetic field with respect to the crystal structure in the two configurations and the international space group representation of FMO is pasted on the right-hand side of the figure. The THz probe is characterized by the $\boldsymbol{k}$ vector, which breaks the set of symmetry operations $\{2_\perp, m_\perp, \bar{1}, 1'\}$. The space group of FMO is $I41/amd$, from the chapter on crystallography in this thesis we know that the Bravais lattice of this crystal has an inversion center, and the inversion symmetry is broken by including the motifs on each lattice site, but it still preserves the $2_\perp$, $m_\perp$ and $1'$ symmetries. But if we launch a magnetic field $\boldsymbol{B}$ along [111] direction of the crystal in the Faraday geometry as shown in figure 12.5, one can find that the whole system including the magnetic field breaks the $2_\perp$, $m_\perp$ and $1'$ symmetries simultaneously, then from the perspective of SOS, FMO crystal with the $\boldsymbol{B}$ field in Faraday geometry should exhibit non-reciprocal effect. While for the Voigt geometry, the external magnetic field is perpendicular to the [111] direction of the crystal, the SOS analysis result turns out to be conditional. (1) If the magnetic field $\boldsymbol{B}$ lies in the ac plane or the bc plane of the

crystal structure, then the specimen which including the crystal and the magnetic field still maintains the $m_\perp$ and $2_\perp$ symmetries, so the THz light should be reciprocal. (2) If the magnetic field $\boldsymbol{B}$ is out of the ac plane and bc plane, then all the symmetries in the set $\{2_\perp, m_\perp, \bar{1}, 1'\}$ are broken, then this configuration is predicted to have THz non-reciprocal effect. But from our experiment results, we only observed THz reciprocal phenomenon instead of both in the Voigt geometry. It is possible that we accidentally aligned the magnetic field $\boldsymbol{B}$ in the ac or bc plane, but it is more possible that some other mechanism stops it from being so and this should be examined by the future investigation.

12.4 Summary

In summary, we conducted THz transmission and ellipticity measurement on FMO in Faraday and Voigt geometries. We studied the magnetic spin resonance at $3K$ and $40K$ under various magnetic field. THz non-reciprocal effect is observed in the Faraday geometry configuration but not in the Voigt geometry. We anaylised the symmetry of the experiment by SOS method, the THz non-reciprocal effect in Faraday geometry is predicted readily from the perspective of SOS, while for the Voigt geometry, the result is conditional, further investigation is needed to fully understand it.

Bibliography

[1] Daniel C. Harris and Michael D.Bertolucci. *Symmetry and spectroscopy: an introduction to vibrational and electronic spectroscopy*. Dover publications, 1989. ISBN 048666144X.

[2] George Turrell. *Infrared and Raman Spectra of Crystal*. ACADEMY PRESS INC. LTD., 1972. ISBN 0127050507.

[3] Joseph A. Gallian. *Contemporary abstract algebra*. Cengage learning, 2013. ISBN 9781133599708.

[4] Jacobs university. Character tables for chemically important point groups. URL http://symmetry.jacobs-university.de/.

[5] Ashcroft and Mermin. *Solid state physics*. physics. Cengage learning, 2017. ISBN 9788131500521.

[6] Frank Hoffmann. *Introduction to Crystallography*. Inorganic chemistry. Springer International Publishing, 2020. ISBN 978-3-030-35110-6.

[7] Stefan A. Maier. *Plasmonics: Fundamentals and Applications*. Springer, 2007. ISBN 0-387-33150-6.

[8] Yun-Shik Lee. *Principles of Terahertz Science and Technology*. New York, NY: Springer-Verlag, 2009. ISBN 9780387095394.

[9] Mark Fox. *Optical properties of solids*. Oxford master series in condensed matter physics. Oxford University Press, 1972. ISBN 9780199573363.

[10] Grant R. Fowles. *Introduction to Modern Optics*. Optics. Dover publications, 1989. ISBN 0-486-65957-7.

[11] E.M. Lifshitz L.D. Landau and L.P. Pitaevskii. *Electrodynamics of Continuous Media*. Elsevier Butterworth-Heinemann Publications, 1984. ISBN 0750626348.

[12] Satoshi Tomita, Hiroyuki Kurosawa, Tetsuya Ueda, and Kei Sawada. Metamaterials with magnetism and chirality. *Journal of Physics D: Applied Physics*, 51(8):083001, 2018. doi: 10.1088/1361-6463/aa9ecb. URL https://doi.org/10.1088/1361-6463/aa9ecb.

[13] Hiroyuki Kurosawa and Shin-ichiro Inoue. Born-kuhn model for magnetochiral effects. *Phys. Rev. A*, 98:053805, Nov 2018. doi: 10.1103/PhysRevA.98.053805. URL https://link.aps.org/doi/10.1103/PhysRevA.98.053805.

[14] Dávid Szaller, Sándor Bordács, and István Kézsmárki. Symmetry conditions for nonreciprocal light propagation in magnetic crystals. *Phys. Rev. B*, 87:014421, Jan 2013. doi: 10.1103/PhysRevB.87.014421. URL https://link.aps.org/doi/10.1103/PhysRevB.87.014421.

[15] G. L. J. A. Rikken, C. Strohm, and P. Wyder. Observation of magnetoelectric directional anisotropy. *Phys. Rev. Lett.*, 89:133005, Sep 2002. doi: 10.1103/PhysRevLett.89.133005. URL https://link.aps.org/doi/10.1103/PhysRevLett.89.133005.

[16] Kei Sawada and Naoto Nagaosa. Optical magnetoelectric effect in multiferroic materials: Evidence for a lorentz force acting on a ray of light. *Phys. Rev. Lett.*, 95:237402, Dec 2005. doi: 10.1103/PhysRevLett.95.237402. URL https://link.aps.org/doi/10.1103/PhysRevLett.95.237402.

[17] J. Hlinka. Eight types of symmetrically distinct vectorlike physical quantities. *Phys. Rev. Lett.*, 113:165502, Oct 2014. doi: 10.1103/PhysRevLett.113.165502. URL https://link.aps.org/doi/10.1103/PhysRevLett.113.165502.

[18] Shukai Yu, Bin Gao, Jae Wook Kim, Sang-Wook Cheong, Michael K. L. Man, Julien Madéo, Keshav M. Dani, and Diyar Talbayev. High-temperature terahertz optical diode effect without magnetic order in polar $feznmo_3o_8$. *Phys. Rev. Lett.*, 120:037601, Jan 2018. doi: 10.1103/PhysRevLett.120.037601. URL https://link.aps.org/doi/10.1103/PhysRevLett.120.037601.

[19] S. Bordacs, I. Kézsmárki, S. Seki, and Y. Tokura. Chirality of matter shows up via spin excitations. *Nat. Comm.*, 5:4583, 2014. doi: 10.1038/ncomms5583. URL http://dx.doi.org/10.1038/ncomms5583.

[20] Sang-Wook Cheong, Diyar Talbayev, Valery Kiryukhin, and Avadh Saxena. Broken symmetries, non-reciprocity, and multiferroicity. *npj Quantum Materials*, 3(1):19, 2018. ISSN 2397-4648. doi: 10.1038/s41535-018-0092-5. URL https://doi.org/10.1038/s41535-018-0092-5.

[21] Sang-Wook Cheong. SOS: symmetry-operational similarity. *npj Quantum Materials*, 4(1):53, 2019. ISSN 2397-4648. doi: 10.1038/s41535-019-0193-9. URL https://doi.org/10.1038/s41535-019-0193-9.

[22] Stephen Blundell. *Magnetism in condensed matter*. Oxford master series in condensed matter physics. Oxford university press, 2001. ISBN 9780198505921.

[23] H.C.Siegmann J.Stohr. *Magnetism from fundamentals to nanoscale dynamics*. Solid-state sciences. Springer, 2006. ISBN 103540302824.

[24] Roshan Kumar Nepal. Investigation of complex magnetic phenomena in spinel femn2o4, mnfe2o4, and nife2o4. *LSU doctoral dissertation*, 2020.

[25] Charles Kittel. *Introduction to solid state physics*. John Wiley & sons, Inc, 2005. ISBN 047141526X.

[26] Charles Kittel. Interpretation of anomalous larmor frequencies in ferromagnetic resonance experiment. *Phys. Rev.*, 71:270–271, 2 1947. doi: 10.1103/PhysRev.71.270.2. URL https://link.aps.org/doi/10.1103/PhysRev.71.270.2.

[27] J. H. E. GRIFFITHS. Anomalous high-frequency resistance of ferromagnetic metals. *Nature*, 158(4019):670–671, 1946. ISSN 1476-4687. doi: 10.1038/158670a0. URL https://doi.org/10.1038/158670a0.

[28] T. Seifert, S. Jaiswal, U. Martens, J. Hannegan, L. Braun, P. Maldonado, F. Freimuth, A. Kronenberg, J. Henrizi, I. Radu, E. Beaurepaire, Y. Mokrousov, P. M. Oppeneer, M. Jourdan, G. Jakob, D. Turchinovich, L. M. Hayden, M. Wolf, M. Münzenberg, M. Kläui, and T. Kampfrath. Efficient metallic spintronic emitters of ultrabroadband terahertz radiation. *Nature Photonics*, 10(7):483–488, 2016. ISSN 1749-4893. doi: 10.1038/nphoton.2016.91. URL https://doi.org/10.1038/nphoton.2016.91.

[29] T. Kampfrath, M. Battiato, P. Maldonado, G. Eilers, J. Nötzold, S. Mährlein, V. Zbarsky, F. Freimuth, Y. Mokrousov, S. Blügel, M. Wolf, I. Radu, P. M.

Oppeneer, and M. Münzenberg. Terahertz spin current pulses controlled by magnetic heterostructures. *Nature Nanotechnology*, 8(4):256–260, 2013. ISSN 1748-3395. doi: 10.1038/nnano.2013.43. URL https://doi.org/10.1038/nnano.2013.43.

[30] Liang Cheng, Ziqi Li, Daming Zhao, and Elbert E. M. Chia. Studying spin–charge conversion using terahertz pulses. *APL Materials*, 9(7):070902, 2021. doi: 10.1063/5.0051217. URL https://doi.org/10.1063/5.0051217. _eprint: https://doi.org/10.1063/5.0051217.

[31] Takashi Arikawa, Xiangfeng Wang, Alexey A. Belyanin, and Junichiro Kono. Giant tunable faraday effect in a semiconductor magneto-plasma for broadband terahertz polarization optics. *Opt. Express*, 20(17):19484–19492, 2012. doi: 10.1364/OE.20.019484. URL http://opg.optica.org/oe/abstract.cfm?URI=oe-20-17-19484. Publisher: OSA.

[32] L. Duvillaret, F. Garet, and J.-L. Coutaz. A reliable method for extraction of material parameters in terahertz time-domain spectroscopy. *IEEE Journal of Selected Topics in Quantum Electronics*, 2(3):739–746, 1996. doi: 10.1109/2944.571775.

[33] Xian Li, Tian Qiu, Jiahao Zhang, Edoardo Baldini, Jian Lu, Andrew M. Rappe, and Keith A. Nelson. Terahertz field–induced ferroelectricity in quantum paraelectric SrTiO3. *Science*, 364(6445):1079–1082, 2019. ISSN 0036-8075. doi: 10.1126/science.aaw4913. URL https://science.sciencemag.org/content/364/6445/1079. Publisher: American Association for the Advancement of Science _eprint: https://science.sciencemag.org/content/364/6445/1079.full.pdf.

[34] M. Först, C. Manzoni, S. Kaiser, Y. Tomioka, Y. Tokura, R. Merlin, and A. Cavalleri. Nonlinear phononics as an ultrafast route to lattice control. *Nature Physics*, 7(11):854–856, 2011. ISSN 1745-2481. doi: 10.1038/nphys2055. URL https://doi.org/10.1038/nphys2055.

[35] Naoki Sono, Yuto Kinoshita, Noriaki Kida, Toshimitsu Ito, Hiroshi Okamoto, and Tatsuya Miyamoto. Terahertz-field-induced changes of electronic states associated with a polarization modulation in BiFeO3. *Journal of the Physical Society of Japan*, 90(3):033703, 2021. doi: 10.7566/JPSJ.90.033703. URL https://doi.org/10.7566/JPSJ.90.033703. _eprint: https://doi.org/10.7566/JPSJ.90.033703.

[36] Sergey Prosandeev, Julie Grollier, Diyar Talbayev, Brahim Dkhil, and L. Bellaiche. Ultrafast neuromorphic dynamics using hidden phases in the prototype of relaxor ferroelectrics. *Phys. Rev. Lett.*, 126:027602, Jan 2021. doi: 10.1103/PhysRevLett.126.027602. URL `https://link.aps.org/doi/10.1103/PhysRevLett.126.027602`.

[37] M. Kozina, M. Fechner, P. Marsik, T. van Driel, J. M. Glownia, C. Bernhard, M. Radovic, D. Zhu, S. Bonetti, U. Staub, and M. C. Hoffmann. Terahertz-driven phonon upconversion in SrTiO3. *Nature Physics*, 15(4): 387–392, 2019. ISSN 1745-2481. doi: 10.1038/s41567-018-0408-1. URL `https://doi.org/10.1038/s41567-018-0408-1`.

[38] Alaska Subedi, Andrea Cavalleri, and Antoine Georges. Theory of nonlinear phononics for coherent light control of solids. *Phys. Rev. B*, 89(22): 220301, 2014. doi: 10.1103/PhysRevB.89.220301. URL `https://link.aps.org/doi/10.1103/PhysRevB.89.220301`. Publisher: American Physical Society.

[39] Alaska Subedi. Proposal for ultrafast switching of ferroelectrics using midinfrared pulses. *Phys. Rev. B*, 92:214303, Dec 2015. doi: 10.1103/PhysRevB.92.214303. URL `https://link.aps.org/doi/10.1103/PhysRevB.92.214303`.

[40] Ghenadii D. Stojanovic, Biljana ; Korotcenkov. *Magnetic, Ferroelectric, and Multiferroic Metal Oxides*. Metal Oxides Series. Saint Louis: Elsevier, 2018. ISBN 9780128111802.

[41] J. Petzelt. Soft mode behavior in cubic and tetragonal batio3 crystals and ceramics: Review on the results of dielectric spectroscopy. *Ferroelectrics*, 375(1):156–164, 2008. doi: 10.1080/00150190802438009. URL `https://doi.org/10.1080/00150190802438009`. Publisher: Taylor & Francis.

[42] G. Shirane, R. Nathans, and V. J. Minkiewicz. Temperature dependence of the soft ferroelectric mode in ktao$_3$. *Phys. Rev.*, 157:396–399, May 1967. doi: 10.1103/PhysRev.157.396. URL `https://link.aps.org/doi/10.1103/PhysRev.157.396`.

[43] H. Uwe, K. B. Lyons, H. L. Carter, and P. A. Fleury. Ferroelectric microregions and raman scattering in ktao$_3$. *Phys. Rev. B*, 33:6436–6440, May

1986. doi: 10.1103/PhysRevB.33.6436. URL `https://link.aps.org/doi/` `10.1103/PhysRevB.33.6436`.

[44] Yoshiaki Uesu, Ryuhei Nakai, Jean-Michel Kiat, Carole Ménoret, Mitsuru Itoh, and Toru Kyomen. Polar order in quantum paraelectric SrTi16o3 and SrTi18o3 at low temperature. *Journal of the Physical Society of Japan*, 73(5): 1139–1142, 2004. doi: 10.1143/JPSJ.73.1139. URL `https://doi.org/10.` `1143/JPSJ.73.1139`. _eprint: https://doi.org/10.1143/JPSJ.73.1139.

[45] Ulrich Aschauer and Nicola A. Spaldin. Competition and cooperation between antiferrodistortive and ferroelectric instabilities in the model perovskite SrTiO3. *Journal of Physics: Condensed Matter*, 26(12):122203, 2014. doi: 10.1088/0953-8984/26/12/122203. URL `https://doi.org/10.1088/` `0953-8984/26/12/122203`. Publisher: IOP Publishing.

[46] Robert C. Miller and William G. Spitzer. Far infrared dielectric dispersion in ktao$_3$. *Phys. Rev.*, 129:94–98, Jan 1963. doi: 10.1103/PhysRev.129.94. URL `https://link.aps.org/doi/10.1103/PhysRev.129.94`.

[47] Hans Vogt and Hiromoto Uwe. Hyper-raman scattering from the incipient ferroelectric ktao$_3$. *Phys. Rev. B*, 29:1030–1034, Jan 1984. doi: 10.1103/ PhysRevB.29.1030. URL `https://link.aps.org/doi/10.1103/PhysRevB.` `29.1030`.

[48] P. A. Fleury and J. M. Worlock. Electric-field-induced raman scattering in srtio$_3$ and ktao$_3$. *Phys. Rev.*, 174:613–623, Oct 1968. doi: 10.1103/PhysRev. 174.613. URL `https://link.aps.org/doi/10.1103/PhysRev.174.613`.

[49] C. H. Perry, Jeanne H. Fertel, and T. F. McNelly. Temperature dependence of the raman spectrum of SrTiO3 and KTaO3. *The Journal of Chemical Physics*, 47(5):1619–1625, 1967. doi: 10.1063/1.1712142. URL `https://doi.` `org/10.1063/1.1712142`. _eprint: https://doi.org/10.1063/1.1712142.

[50] P. D. C. King, R. H. He, T. Eknapakul, P. Buaphet, S.-K. Mo, Y. Kaneko, S. Harashima, Y. Hikita, M. S. Bahramy, C. Bell, Z. Hussain, Y. Tokura, Z.-X. Shen, H. Y. Hwang, F. Baumberger, and W. Meevasana. Subband structure of a two-dimensional electron gas formed at the polar surface of the strong spin-orbit perovskite ktao$_3$. *Phys. Rev. Lett.*, 108:117602, Mar 2012. doi: 10.1103/PhysRevLett.108.117602. URL `https://link.aps.org/` `doi/10.1103/PhysRevLett.108.117602`.

[51] K. Ueno, S. Nakamura, H. Shimotani, H. T. Yuan, N. Kimura, T. Nojima, H. Aoki, Y. Iwasa, and M. Kawasaki. Discovery of superconductivity in KTaO3 by electrostatic carrier doping. *Nature Nanotechnology*, 6(7):408–412, 2011. ISSN 1748-3395. doi: 10.1038/nnano.2011.78. URL `https://doi.org/10.1038/nnano.2011.78`.

[52] Yi Yang, Chen-Sheng Lin, Jin-Feng Chen, Lei Hu, and Wen-Dan Cheng. Ferromagnetic-nonmagnetic and metal-insulator phase transitions at the interfaces of KTaO3 and PbTiO3. *Journal of Applied Physics*, 116(15):153709, 2014. doi: 10.1063/1.4898738. URL `https://doi.org/10.1063/1.4898738`. _eprint: https://doi.org/10.1063/1.4898738.

[53] Yuki Ichikawa, Masaya Nagai, and Koichiro Tanaka. Direct observation of the soft-mode dispersion in the incipient ferroelectric KTaO3. *Phys. Rev. B*, 71(9):092106, March 2005. doi: 10.1103/PhysRevB.71.092106. URL `https://link.aps.org/doi/10.1103/PhysRevB.71.092106`.

[54] Chen Ang, A. S. Bhalla, and L. E. Cross. Dielectric behavior of paraelectric $\mathrm{KTaO_3,}$ $\mathrm{CaTiO_3,}$ and $(ln_{1/2}\mathrm{Na_{1/2})}\mathrm{TiO_3}$ under a dc electric field. *Phys. Rev. B*, 64(18):184104, 2001. doi: 10.1103/PhysRevB.64.184104. URL `https://link.aps.org/doi/10.1103/PhysRevB.64.184104`. Publisher: American Physical Society.

[55] K. A. Müller and H. Burkard. Srtio$_3$: An intrinsic quantum paraelectric below 4 k. *Phys. Rev. B*, 19:3593–3602, Apr 1979. doi: 10.1103/PhysRevB.19.3593. URL `https://link.aps.org/doi/10.1103/PhysRevB.19.3593`.

[56] Shuai Lin, Shukai Yu, and Diyar Talbayev. Measurement of quadratic terahertz optical nonlinearities using second-harmonic lock-in detection. *Phys. Rev. Applied*, 10:044007, Oct 2018. doi: 10.1103/PhysRevApplied.10.044007. URL `https://link.aps.org/doi/10.1103/PhysRevApplied.10.044007`.

[57] George Turrel. *Infrared and Raman Spectra of Crystals*. Spectroscopy and Spectrum Analysis. London, New York, Academic Press, 1972. ISBN 0127050507.

[58] Marco A. Allodi, Ian A. Finneran, and Geoffrey A. Blake. Nonlinear terahertz coherent excitation of vibrational modes of liquids. *The Journal of Chemical Physics*, 143(23):234204, 2015. doi: 10.

1063/1.4938165. URL `https://doi.org/10.1063/1.4938165`. _eprint: https://doi.org/10.1063/1.4938165.

[59] L. D. Barron. *Molecular light scattering and optical activity*. Cambridge university press, 2004. ISBN 9780511231216.

[60] M.V. Hobden. Optical activity in a non-enantiomorphous crystal: *aggas₂*. *Acta Christ.*, 24:676, 1968. URL `https://scripts.iucr.org/cgi-bin/paper?a05985`.

[61] S. Bordács, I. Kézsmárki, D. Szaller, L. Demkó, N. Kida, H. Murakawa, Y. Onose, R. Shimano, T. Rõõm, U. Nagel, S. Miyahara, N. Furukawa, and Y. Tokura. Chirality of matter shows up via spin excitations. *Nature Physics*, 8(10):734–738, 2012. ISSN 1745-2481. doi: 10.1038/nphys2387. URL `https://doi.org/10.1038/nphys2387`.

[62] Edward C. Hsu and G. Holzwarth. Vibrational circular dichroism observed in crystalline. *The Journal of Chemical Physics*, 59(9):4678–4685, 1973. doi: 10.1063/1.1680680. URL `https://doi.org/10.1063/1.1680680`. _eprint: https://doi.org/10.1063/1.1680680.

[63] B. Liu and J. Barbier. Structures of the stuffed tridymite derivatives, BaMSiO4 (m = co, zn, mg). *Journal of Solid State Chemistry*, 102(1):115–125, 993. ISSN 0022-4596. doi: https://doi.org/10.1006/jssc.1993.1013. URL `https://www.sciencedirect.com/science/article/pii/S0022459683710133`.

[64] J. Anike, R. Derbeshi, W. Wong-Ng, W. Liu, D. Windover, N. King, S. Wang, J. A. Kaduk, and Y. Lan. Structural and optical properties of bczso. *Powder Diffraction*, 34(3):242–250, 2019. doi: 10.1017/S0885715619000447.

[65] Hiroki Taniguchi, Hiroki Moriwake, Akihide Kuwabara, Takuma Okamura, Takafumi Yamamoto, Ryuji Okazaki, Mitsuru Itoh, and Ichiro Terasaki. Photo-induced change of dielectric response in BaCoSiO4 stuffed tridymite. *Journal of Applied Physics*, 115(16):164103, 2014. doi: 10.1063/1.4872032. URL `https://doi.org/10.1063/1.4872032`. _eprint: https://doi.org/10.1063/1.4872032.

[66] Lei Ding, Xianghan Xu, Harald O. Jeschke, Xiaojian Bai, Erxi Feng, Admasu Solomon Alemayehu, Jaewook Kim, Fei-Ting Huang, Qiang Zhang, Xiaxin Ding, Neil Harrison, Vivien Zapf, Daniel Khomskii, Igor I. Mazin,

Sang-Wook Cheong, and Huibo Cao. Field-tunable toroidal moment in a chiral-lattice magnet. *Nature Communications*, 12(1):5339, 2021. ISSN 2041-1723. doi: 10.1038/s41467-021-25657-6. URL `https://doi.org/10.1038/s41467-021-25657-6`.

[67] Shukai Yu, C. Dhanasekhar, Venimadhav Adyam, Skylar Deckoff-Jones, Michael K. L. Man, Julien Madéo, E Laine Wong, Takaaki Harada, M. Bala Murali Krishna, Keshav M. Dani, and Diyar Talbayev. Terahertz-frequency magnetoelectric effect in ni-doped cabaco$_4$o$_7$. *Phys. Rev. B*, 96:094421, Sep 2017. doi: 10.1103/PhysRevB.96.094421. URL `https://link.aps.org/doi/10.1103/PhysRevB.96.094421`.

[68] K. H. Weyrich. "frozen" phonon calculations: Lattice dynamics and -instabilities. *Ferroelectrics*, 104(1):183–194, 1990. doi: 10.1080/00150199008223822. URL `https://doi.org/10.1080/00150199008223822`. Publisher: Taylor & Francis _eprint: https://doi.org/10.1080/00150199008223822.

[69] Atsushi Togo and Isao Tanaka. First principles phonon calculations in materials science. *Scripta Materialia*, 108:1–5, 2015. ISSN 1359-6462. doi: https://doi.org/10.1016/j.scriptamat.2015.07.021. URL `https://www.sciencedirect.com/science/article/pii/S1359646215003127`.

[70] David Santos-Carballal, Alberto Roldan, Ricardo Grau-Crespo, and Nora H. de Leeuw. First-principles study of the inversion thermodynamics and electronic structure of FeM_2X_4 (thio)spinels (m = Cr, mn, co, ni; x = O, s). *Phys. Rev. B*, 91:195106, 5 2015. doi: 10.1103/PhysRevB.91.195106. URL `https://link.aps.org/doi/10.1103/PhysRevB.91.195106`.

[71] R. A. de Groot, F. M. Mueller, P. G. van Engen, and K. H. J. Buschow. New class of materials: Half-metallic ferromagnets. *Phys. Rev. Lett.*, 50:2024–2027, 6 1983. doi: 10.1103/PhysRevLett.50.2024. URL `https://link.aps.org/doi/10.1103/PhysRevLett.50.2024`.

[72] Anubhav Jain, Shyue Ping Ong, Geoffroy Hautier, Wei Chen, William Davidson Richards, Stephen Dacek, Shreyas Cholia, Dan Gunter, David Skinner, Gerbrand Ceder, and Kristin a. Persson. The Materials Project: A materials genome approach to accelerating materials innovation. *APL Materials*, 1(1):011002, 2013. ISSN 2166532X. doi:

10.1063/1.4812323. URL `http://link.aip.org/link/AMPADS/v1/i1/`
`p011002/s1&Agg=doi`.

[73] Roshan Nepal, Qiang Zhang, Samuel Dai, Wei Tian, S. E. Nagler, and Rongying Jin. Structural and magnetic transitions in spinel FeMn$_2$o$_4$ single crystals. *Phys. Rev. B*, 97:024410, 1 2018. doi: 10.1103/PhysRevB.97.024410. URL `https://link.aps.org/doi/10.1103/PhysRevB.97.024410`.